

## The history of soil gleyization in the Songnen Plain over the last 195 ka, as revealed by the Harbin loess-paleosol sequence, NE China

Yujia Sun <sup>a,1</sup>, Yanru Wang <sup>a,b,\*</sup>, Yuanyun Xie <sup>a,b,\*1</sup>, Chunguo Kang <sup>c</sup>, Chuanyi Wei <sup>d,\*\*</sup>,  
Yehui Wang <sup>a</sup>, Jie Meng <sup>a,b</sup>, Lei Sun <sup>a,b</sup>, Peng Wu <sup>e</sup>, Ruonan Liu <sup>f</sup>, Zhenyu Wei <sup>a</sup>, Haijin Liu <sup>a</sup>,  
Yunping Chi <sup>a,b</sup>

<sup>a</sup> College of Geographic Science, Harbin Normal University, Harbin 150025, China

<sup>b</sup> Heilongjiang Province Key Laboratory of Geographical Environment Monitoring and Spatial Information Service in Cold Regions, Harbin Normal University, Harbin 150025, China

<sup>c</sup> College of Geography and Tourism, Harbin University, Harbin 150086, China

<sup>d</sup> State Key Laboratory of Earthquake Dynamics and Forecasting, Institute of Geology, China Earthquake Administration, Beijing 100029, China

<sup>e</sup> School of Earth Sciences and Spatial Information Engineering, Hunan University of Science and Technology, Xiangtan 411201, China

<sup>f</sup> School of Environmental Studies, China University of Geosciences (Wuhan), Wuhan 430078, China

### ARTICLE INFO

Editor: P Srivastava

**Keywords:**

Harbin loess

Hm/Gt ratio

Magnetic susceptibility

Gleyization degree

Songnen Plain

### ABSTRACT

Understanding the spatiotemporal evolution patterns of East Asian summer monsoon (EASM) precipitation and its forcing mechanisms is essential for comprehending global climate change and regional environmental shifts. Despite this significance, a lack of well-exposed outcrop sections has constrained our understanding of the evolution and forcing mechanisms of the EASM in the Songnen Plain, NE China. To address this critical issue, this study conducted a high-resolution analysis of magnetic susceptibility, goethite (Gt), and hematite (Hm) in the Harbin loess-paleosol sequence located in the southeastern Songnen Plain. In addition, a close-spaced OSL and ESR dating was employed, with the primary aim of unraveling the paleoclimatic significance of these proxies in the uniquely developed black paleosol regions of the cold climate. The results indicate that the black paleosol layers exhibit significantly lower values of low-frequency magnetic susceptibility ( $\chi_{lf}$ ), goethite (Gt) and hematite (Hm) compared to the loess layers, indicating a decoupling between these indicators and the pedogenic processes. These findings imply that gleyization has influenced the Harbin black paleosol layers during their development. Furthermore, a negative correlation was observed ( $R^2 = 0.65$  for  $\chi_{lf}$  and  $R^2 = 0.42$  for Hm/Gt ratio) between the  $\chi_{lf}$  and the Hm/Gt ratio of the topsoil in potential dust sources, and mean annual precipitation (MAP). Consequently, the  $\chi_{lf}$ -MAP and Hm/Gt-MAP climofunctions were proposed to reconstruct the paleoprecipitation recorded by the Harbin loess-paleosol sequence. The differences in precipitation, as constructed by  $\chi_{lf}$  and Hm/Gt, can be used to characterize the degree in gleyization of the black paleosol. Based on the quantitative reconstruction of paleoprecipitation and paleogleyization, the paleoclimatic evolution of the Songnen Plain since 195 ka can be categorized into three stages: from 195 to 160 ka, the East Asian summer monsoon (EASM) was strong, characterized by a cold and wet climate and a low degree of soil gleyization; from 160 ka to 123 ka, the intensity of the EASM weakened, with the warm and dry climate, as well as an increased degree of soil gleyization; after 123 ka, monsoon precipitation continued to decline, the climate became cool and dry, and the rate of permafrost melting slowed; however, from 105 to 100 ka, a modest increase in temperature and monsoon rainfall occurred, accompanied by intensified soil gleyization; in contrast, from 65 to 55 ka, the climate resembled that of the earlier cold interval. Overall, the evolution of summer monsoon precipitation in the Songnen Plain is jointly regulated by both high- and low-latitude processes. The summer solar radiation and changes in Arctic ice volume are the main factors affecting the evolution of the EASM. Additionally, the Western

\* Corresponding author at: College of Geographic Science, Harbin Normal University, Harbin 150025, China.

\*\* Corresponding author.

E-mail addresses: [wangyr050607@126.com](mailto:wangyr050607@126.com) (Y. Wang), [xyy0451@163.com](mailto:xyy0451@163.com) (Y. Xie), [chuanyiwei@ies.ac.cn](mailto:chuanyiwei@ies.ac.cn) (C. Wei).

<sup>1</sup> These authors contributed equally to this work.

Pacific Subtropical High (WPSH) or El Niño-Southern Oscillation (ENSO) events also contribute to the variations in monsoon precipitation to some extent.

## 1. Introduction

The extensive distribution and ongoing accumulation of loess deposits have made them one of the most effective archives for reconstructing the Quaternary paleoclimate and paleoenvironment changes (Lu and An, 1998; Lu and An, 1997). The Chinese loess-paleosol sequences provide a continuous record of paleoclimatic changes and insights into the important issues such as the evolution history of the East Asian monsoon and aridification of arid regions in Asia interior since

approximately 2.6 Ma (Liu, 1985), thus enhancing our comprehension of global paleoclimate dynamics.

Magnetic susceptibility (MS) from the loess-paleosol sequences in the Chinese Loess Plateau (CLP) has been widely employed to understand the East Asian monsoon evolution (Ding et al., 2002; Liu et al., 2012; Liu and Liu, 2013; Liu et al., 2015; Kong et al., 2020). The MS in loess-paleosol sequences exhibits three types of relationships with climate: positive correlation, as observed in the western-central CLP (Heller et al., 1991; Liu et al., 1992; Zhou et al., 1990); anti-correlation, as in the

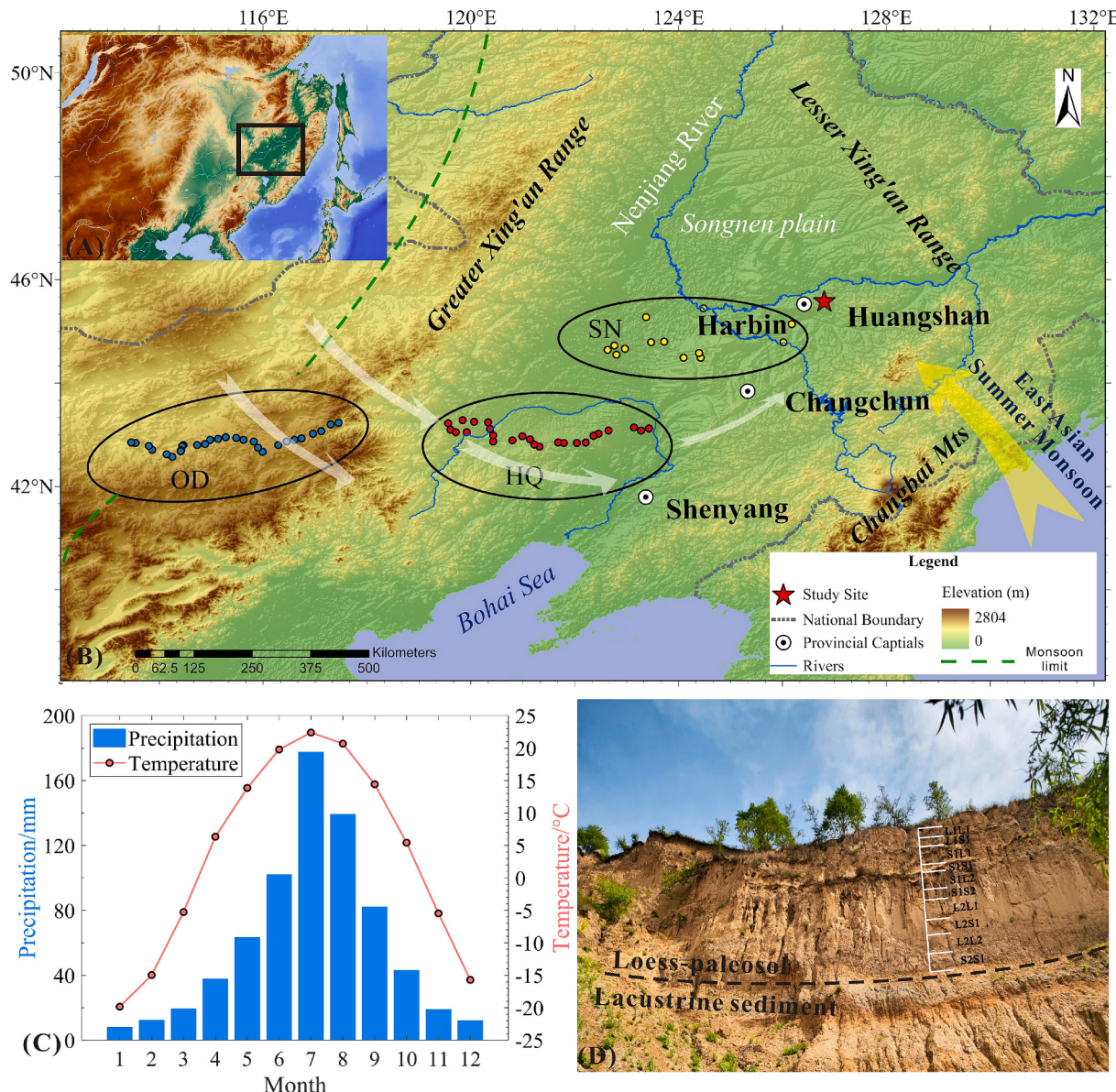


**Fig. 1.** (A) Sketch Map of East Asia, showing location of the study area; (B) DEM map of Northeastern Plain, showing the distribution of Songnen Sandy land (SN), Onqin Daga Sandy Land (OD) and Horqin Sandy Land (HQ) (Wu et al., 2020; Zhang et al., 2023; Liu et al., 2023). The points of different colors within the three sandy lands represent the sampling location. The red five-pointed star represents the location of the HS outcrop section. The white arrow represents the paths of dust transportation (Qiu, 2008). The modern Asian summer monsoon limit is shown by a green dashed line (Gao et al., 1962); (C) Meteorological data (temperature and precipitation) in HS are sourced from observational data at a nearby meteorological station located at 45°35'58"N, 126°48'25.2"E, covering the period from 1971 to 2000. The original data is provided by the Copernicus Climate Change Service (C3S) Climate Data Store (CDS) (Muñoz Sabater, 2019); (D) The profile photographs of the HS loess-paleosol section and includes detailed stratigraphic annotations of loess and paleosol layers. (For interpretation of the references to colour in this figure legend, the reader is referred to the web version of this article.)

case of Siberia and Alaska loess (Liu et al., 2007a, 2008); and non-correlation, as in the case of New Zealand loess (Ma et al., 2013) and Argentine loess (Heil et al., 2010). As a result, the correlation between MS and climate differs geographically, illustrating the complexity of soil magnetic enhancement mechanisms.

The concentration of hematite (Hm) and goethite (Gt) in the loess-paleosol sequences are highly sensitive indicators of climate and environment changes, and have been successfully employed in paleoclimate reconstructions (Balsam et al., 2004; Cornell and Schwertmann, 2003; Ji et al., 2004; Ji et al., 2007; Wang et al., 2016; Jia et al., 2018). Generally, Hm and Gt compete with one another in soil formation processes. Hm forms preferentially in soil conditions with low humidity, while Gt forms in relatively moist soil conditions (Cornell and Schwertmann, 2003; Long et al., 2011; Torrent et al., 1982; Zhao et al., 2024). However, Hm and Gt appear to have complex correlations with climatic factors (temperature and precipitation). For instance, research in some eolian profiles reveals that the primary influences of temperature, but not precipitation, on the formation and preservation of Hm and Gt in a large-scale geographical space (Zhu et al., 2022). In the CLP, the primary climatic control factor for Hm is the annual average temperature (Gao et al., 2018). Consequently, the correlations of Hm and Gt with temperature and precipitation differ across various study areas. Additionally, the Hm/Gt ratio has also been widely used as one of the terrestrial paleoclimate proxies (Ao et al., 2020; Balsam et al., 2004; Hao et al., 2009; Ji et al., 2001; Jia et al., 2018; Lepre and Olsen, 2021). Higher Hm/Gt values signify a dry climate, while lower values represent a humid climate environment (Wu et al., 2018). Modern soil researches have demonstrated a positive correlation between the Hm/Gt ratio and temperature (Schwertmann et al., 1982; Gao et al., 2018). The Hm/Gt ratios of paleosols exhibit higher values than those of loess in the central CLP, which indicated a dry climate during the interglacial period (Ao et al., 2020; Torrent et al., 2007). However, the Hm/Gt ratios in the Luochuan section exhibit a gradual decline since 2.6 million years ago, suggesting that the glacials after the middle-late Pleistocene (0–1.2 Ma) were more humid compared to the interglacials before the Early Pleistocene (1.2–2.6 Ma) (Balsam et al., 2004). This is contrary to the viewpoint of humid interglacials and dry glacials demonstrated by paleoclimatic records from most regions (Beck et al., 2018; Guo et al., 2000; Liu, 1985; Maher and Thompson, 1995; Meng et al., 2018; Sun et al., 2019; Ji et al., 2007; Cao et al., 2019). In this regard, the Hm/Gt ratio has climatic implications in response to regional/local conditions.

The loess deposits in NE China are located at the easternmost edge of the Eurasian loess belt, adjacent to the eastern border of the Asian arid and semi-arid zone. It has been one of the ideal areas for researching the response of loess to cold region climate (Xie et al., 2019). The loess-paleosol sequences in Harbin have garnered significant attention due to their considerable thickness and the distinctive coloration of their paleosols. Distinct from the reddish coloring paleosol in the CLP, the paleosols in the Harbin loess-paleosol sequences are gray-brown, called paleo-black soils (Zhang et al., 2021). The Quaternary permafrost on the Songnen Plain is well developed, yet it has been experiencing a gradual degradation in recent years, largely attributed to the intensifying effects of climate warming (Zhu et al., 2024; Wang and Gong, 2024; Fan et al., 2024). Consequently, the increasing humidity of the soil results in a progressively severe degree of soil gleyization.

The Huangshan (HS) loess-paleosol sequence in Harbin is a representative profile in NE China. Existing research primarily focuses on chronology (Wei, 1979; Sun et al., 1982; Wu et al., 1984; Chu et al., 1988; Ye, 1991), genesis (Pavlinov et al., 1956; Xia et al., 1983; Chu et al., 1988; Cao and Zhu, 2014; Wei et al., 2015; Wu et al., 2020a, 2020b), stratigraphic division (Zhan et al., 2018; Wang et al., 2020b), heavy mineral (Wang et al., 2020a), and geochemical characteristics (Du et al., 2020; Wei et al., 2020; Zhang et al., 2020). However, research on the variations of the heavy minerals Hm and Gt in the loess-paleosol sediments has not yet been conducted, which limits our ability to conduct a comprehensive analysis of the paleoclimate in this region. In

this study, we present high-resolution datasets of MS, Hm, and Gt from the Harbin loess-paleosol sequences. The objectives of this study are to (1) identify the vertical variation characteristics of these indices, (2) investigate their paleoclimatic significance, and (3) discuss the history of monsoon precipitation and soil gleyization in the Songnen Plain, alongside their driving mechanisms in response to global climate change in the cold regions.

### 1.1. Study site and regional environment

The Songnen Plain, located in the central part of the Songliao Basin, is an alluvial-lacustrine plain developed from a Late Mesozoic faulted basin (Qiu, 2008) and constitutes the largest part of the Northeast Plain (Fig. 1B). Geographically, the eastern part of the Songnen Plain is characterized by plateaus, the central part by lowlands, and the western part by piedmont plains. Geomorphologically, it is surrounded by mountains and hills on three sides: the Lesser Xing'an Range to the north and northeast, the Changbai Mts to the east and southeast, and the Greater Xing'an Range to the west and northwest. The Songliao divide separates the Songnen Plain from the Liaohe Plain (Qiu, 2008). During the early to middle Pleistocene, there was an ancient large lake that covered an area of approximately 50,000 km<sup>2</sup> on the Songliao Plain (Zhan et al., 2019). The paleolake gradually dried out, and the Songnen Sandy Land was initiated when the Songliao divide uplifted and the aridification prevailed during the late Middle Pleistocene (Wu et al., 2022; Xie et al., 2020; Sun et al., 2023). Thick Quaternary sediments, up to 100–150 m, accumulated in the Songnen plain due to the alluviation of the Songhua River and the Nenjiang River.

Harbin, situated in the southeast of the Songnen Plain, is tectonically at the north end of the southeastern uplift area in the Mesozoic Songliao fault basin (Xie et al., 2020). The Harbin and adjacent areas geomorphologically exhibit a landscape characterized by a river valley, interfluvial, and piedmont plains (Xie et al., 2018). The climate is significantly dominated by the Siberia-Mongolia northwest airflow in winter, and by the Pacific southwest airflow in summer, with a prevailing southwest wind in spring and northwest wind in winter. The Harbin area is characterized by a semi-humid temperate continental monsoon climate (Wu et al., 2021, 2022), with an annual mean temperature of 3.4 °C and an annual mean precipitation of 523.3 mm (Qiu, 2008). The annual evaporation is low, resulting in an abundant effective precipitation (the difference between annual precipitation and annual evaporation).

## 2. Materials and methods

### 2.1. Sampling

#### 2.1.1. Loess-paleosol sequence sampling

The HS section is located in the northeastern part of Harbin city (45° 47' 24.7" N, 126° 47' 30.2" E), about 16 km away from Harbin, with an elevation of 180 m, and geologically constitutes the second terrace of the Songhua River (Wang, 1993). The exposed Huangshan section is approximately 55.53 m thick and is composed of three deposition series. The lower part, 25.63 m thick, is fluvial and lacustrine deposits with well-developed horizontal bedding; the upper part is an eolian loess-paleosol layer ranging from 29.9 m to 1.63 m (Wei et al., 2015; Wu et al., 2020a, 2020b; Liu et al., 2023; Song et al., 2024), and finally a 1.63-m-thick layer of modern soil caps the sequence (Fig. 1D). The loess-paleosol sequences are formed by the accumulation of dust from Songnen Sandy Land, Onqin Daga Sandy Land, and Horqin Sandy Land (Wu et al., 2020a, 2020b; Zhang et al., 2023a; Liu et al., 2023) (Fig. 1) during the late Middle Pleistocene (Wang et al., 2020b). The stratigraphic nomenclature system adopted in this study follows the conventional chronostratigraphic loess-paleosol sequence naming scheme commonly used in the CLP (An et al., 1989). Specifically, the prefixes (e.g., "L1" in "L1S1") represent the last glacial L1 loess layer in the CLP reference

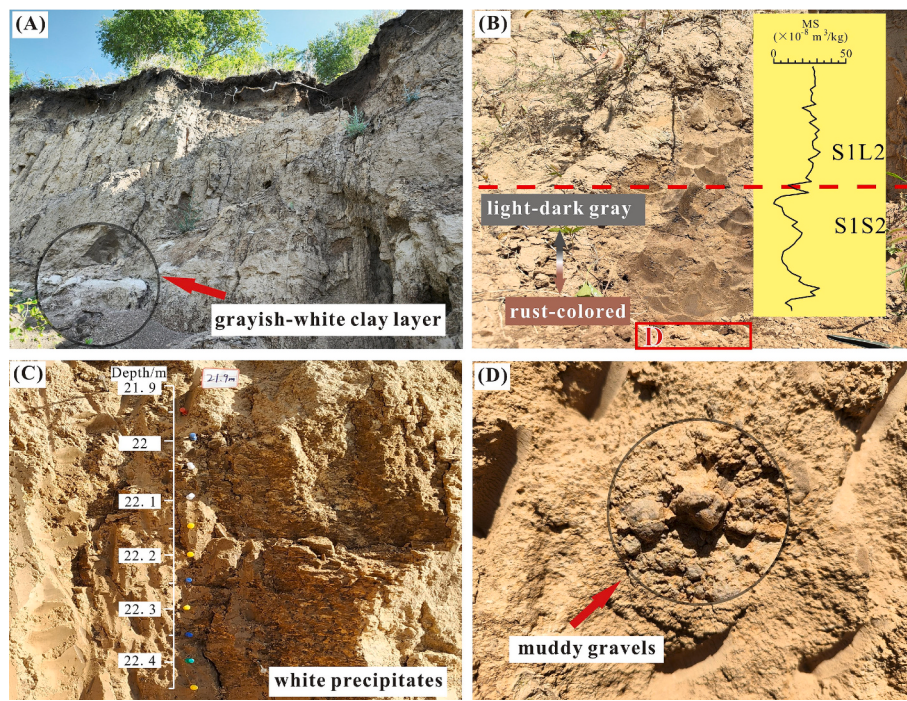


**Fig. 2.** Field photos of the HS loess-paleosol section. (A) A grayish-white clay layer about 0.25 m thick in the middle of L1S1. (B) The colour change of S1S2 paleosols, the lower part is rust-colored paleosol with higher magnetic susceptibility and the upper part turns to light-dark gray with lower magnetic susceptibility (Right-hand curve). (C) White precipitations observed in L2S1. (D) Well-developed muddy gravels.

stratigraphy, while the suffixes (e.g., “S1” in “L1S1”) indicate the first-layer paleosol unit formed in the HS loess section during the last glaciation. Following this convention, the stratigraphic units in this study are designated in descending order as: L1L1, L1S1, S1L1, S1S1, S1L2, S1S2, L2L1, L2S1, L2L2, and S2S1:

- I) S2S1-L2L2: The bottom of the light grayish-brown paleosol layer exhibits strong cohesion, characterized by a small amount of white precipitates and well-developed muddy pebbles. These precipitates gradually disappear upwards, with occasional rust spots. The overlying loess layer exhibits numerous rust spots, and vertical joints are prominent.
- II) L2S1-L2L1: Numerous white precipitates and spots are observed at the bottom of the paleosol layer (Fig. 2C). The soil appears loose and fragmented, and changes to denser and tougher upward. The colour of the paleosol shifts from light grayish-brown to dark grayish-brown, with noticeable iron stains. The loess layer exhibits slight laminae locally, which may have been altered by water flow following deposition.
- III) S1S2-S1L2: The grayish-brown paleosol is fragmented and contains well-developed muddy gravels that are encrusted with white precipitates (Fig. 2D). The overlying loess layer is light yellowish-brown, characterized by iron stains and bluish-gray silt clumps.
- IV) S1S1-S1L1: The light grayish-brown paleosol exhibits no white precipitates or muddy gravel at its base, and similarly, the light yellowish-brown loess lacks any distinct precipitated structures.
- V) L1S1-L1L1: The grayish-brown paleosol is loose and fragmented, characterized by a grayish-white marker layer of approximately 0.25 m thick in the middle. The overlying loess layer is similar to S1L1. Additionally, large muddy balls with outer layers wrapped with white films can be observed in the paleosol (Fig. 2A).

The samples for the indicator analysis were collected at a resolution of 5 cm. Additionally, 11 samples for optically stimulated luminescence (OSL) dating were obtained from depths of 1.9 m, 2.9 m, 3.8 m, 4.4 m,

5.3 m, 6.2 m, 7.1 m, 9.6 m, 10.6 m, 15.7 m and 25.4 m. Furthermore, two samples for electron spin resonance (ESR) dating were collected from depths of 21.75 m and 24.45 m. These dating samples were collected by hammering light-tight steel cylinders (diameter = 8 cm, length = 25 cm) into cleaned vertical sections. The cylinders were then sealed and wrapped using black plastic bags and tape to avoid light exposure and water loss prior to dating.

### 2.1.2. Potential dust source sampling

Previous studies have shown that the loess in Harbin comes from the upward sandy lands, e.g., Onqin Daga Sandy Land (OD), Horqin Sandy Land (HQ), and Songnen Sandy Land (SN), but the contribution of Hulunbuir Sandy Land can be ignored (Wu et al., 2020a, 2020b; Zhang et al., 2023a; Liu et al., 2023). In order to understand the climate implications of indicators and quantitatively reconstruct the paleoclimatic changes, surface sand samples were collected from the dust potential source areas. A total of 17 samples were collected from the SN ( $44^{\circ} \sim 45^{\circ}$ N,  $122^{\circ} \sim 127^{\circ}$ E), 28 samples from the OD ( $42^{\circ} \sim 43^{\circ}$ N,  $112^{\circ} \sim 117^{\circ}$ E), and 25 samples from the HQ ( $42^{\circ} \sim 44^{\circ}$ N,  $119^{\circ} \sim 124^{\circ}$ E). The samples were dry-sieved to obtain  $<63 \mu\text{m}$  fraction for the analysis same as the HS section samples.

## 2.2. Analytical methods

### 2.2.1. Magnetic susceptibility measurement

The air-dried loess-paleosol sequence samples were ground finely into powder by hand, and then placed in weakly magnetic plastic boxes (2 cm per side). Low- and high-frequency magnetic susceptibility ( $\chi_{lf}$  and  $\chi_{hf}$ ) were measured at a low (470 Hz) and high (4700 Hz) frequency in a field of using a Bartington MS2 meter. Each sample was measured three times, and results were averaged. Frequency-dependent magnetic susceptibility ( $\chi_{fd\%}$ ) was calculated from  $\chi_{fd\%} = [(\chi_{lf} - \chi_{hf})/\chi_{lf}] \times 100 \%$ .

### 2.2.2. Diffuse reflectance spectroscopy (DRS)

After natural drying, the sub-samples of the  $<63 \mu\text{m}$  fraction were carried out for the DRS analyses. The instrument was calibrated with

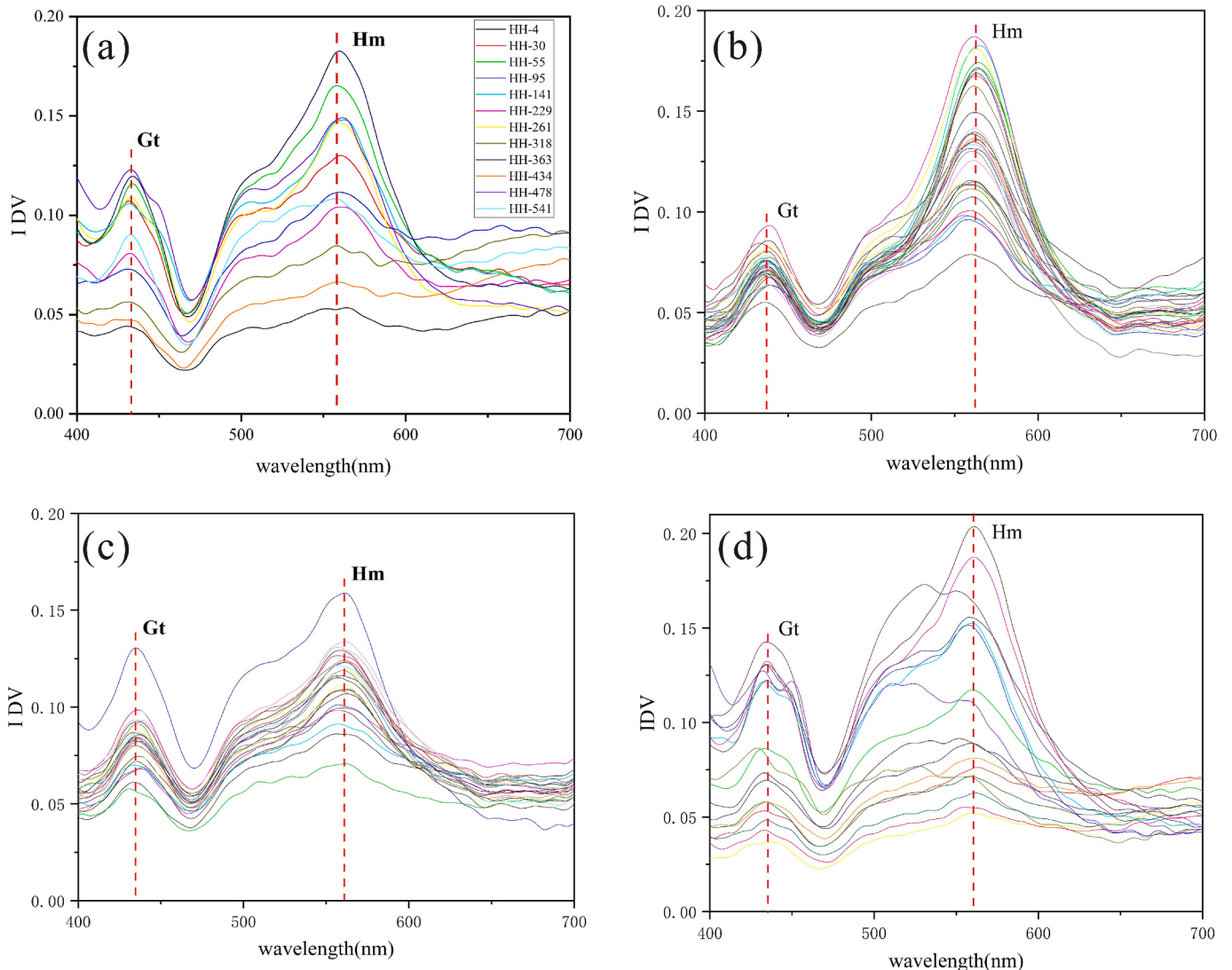


**Fig. 3.** IDV diagrams of loess-paleosol samples from HS loess-paleosol section (The sampling depths are as follows: HH-4 at 0.2 m, HH-30 at 1.5 m, HH-55 at 2.75 m, HH-95 at 4.75 m, HH-141 at 7.05 m, HH-229 at 11.45 m, HH-261 at 13.05 m, HH-318 at 15.90 m, HH-363 at 18.15 m, HH-434 at 21.70 m, HH-478 at 23.90 m, and HH-541 at 27.05 m) (a), and sand samples from OD (b), HQ (c) and SN (d).

BaSO<sub>4</sub> powder before assessment. About 1 g of the treated sample was evenly spread in the test dish and pressed. The Cary 4000 UV-Vis spectrophotometer from Agilent Technologies scanned the visible light spectrum from 300 to 800 nm at 1 nm intervals. Although the second derivative of reflectance (R) processed by the Kubelka-Munk transformation can rapidly estimate the relative contents of hematite (Hm) and goethite (Gt) (Li and Cai, 2014; Yang et al., 2020), our analysis shows that the second derivative DRS spectra for both topsoil and profile samples consistently yielded negative values with significant noise interference. In contrast, the first derivative of DRS (1DV) provides efficient effectively identifies Gt and Hm in soils while minimizing matrix effects. Consequently, we applied first derivative transformation to the reflectance (R%) data to determine the characteristic peak heights of Hm and Gt as proxies for their relative abundances and to calculate the Hm/Gt ratio (Deaton and Balsam, 1991; Ji et al., 2002; Liu et al., 2011). Our results demonstrate that the first derivative spectra (1DV) of loess and surface sediment samples (Fig. 3) exhibit distinct peaks at 435 nm and 565 nm, corresponding to Gt and Hm respectively, which were used to quantify the Hm/Gt ratio (Giosan et al., 2002; Li and Lü, 2024). Notably, the primary peak at 535 nm was excluded due to matrix effects and spectral interference from hematite (Li and Yang, 2012; Jiang and Liu, 2016; Lü et al., 2019). The DRS analysis was conducted at the Key

Laboratory of Photoelectric Bandgap Materials, Ministry of Education, Harbin Normal University.

#### 2.2.3. OSL and ESR dating

In the laboratory darkroom (under safe lighting conditions with weak red light, central wavelength 660 nm), the outer 2–3 cm layer of the sample—potentially exposed or contaminated during sampling or transportation—was removed, after which approximately 50 g of inner unexposed material was extracted for water content and radionuclide concentration measurements, while an additional 100 g was collected for equivalent dose (De) determination. Carbonates and organic matter were subsequently eliminated through sequential treatment with HCl and H<sub>2</sub>O<sub>2</sub> in the darkroom, followed by rinsing with deionized water, isolation of target grain sizes via magnetic separation and heavy-liquid density extraction, and final purification by etching with HF or H<sub>2</sub>SiF<sub>6</sub> before thorough washing and drying for analysis. For 4–11 µm quartz grains, the equivalent dose for quartz was measured using the SAR protocol (Murray and Wintle, 2000), 4–11 µm K-feldspar grains, the equivalent dose for feldspar was measured using the two-step post-IR IRSL (pIRIR) protocol (Thiel et al., 2011), 63–90 µm K-feldspar grains, the equivalent dose for quartz was measured using the SAR PIRIR<sub>225</sub> (Thiel et al., 2011). OSL measurements were made for determining the

**Table 1**

OSL Dating Results of the HS loess-paleosol section.

Sample No.	Depth (m)	Grain size (μm)	U/ppm	Th/ppm	K/%	Water content (%)	Dose Rate (Gy/ka)	De (Gy)	OSL/Age(ka)	mineral
OSL-H12	1.9	4–11	2.19 ± 0.04	11.1 ± 0.1	2.25 ± 0.04	10	3.94 ± 0.19	134.01 ± 3.39	34.01 ± 1.87	Q
OSL-H9	2.9	4–11	2.02 ± 0.08	11.6 ± 0.35	2.42 ± 0.02	10	4.08 ± 0.2	141.53 ± 4.07	34.71 ± 2.00	Q
OSL-H6	3.8	4–11	2.22 ± 0.08	12.4 ± 0.47	2.32 ± 0.02	10	4.1 ± 0.22	150.97 ± 4.51	36.785 ± 2.255	Q
OSL-H4	4.4	4–11	2.19 ± 0.09	11.4 ± 0.31	2.13 ± 0.02	11	3.78 ± 0.2	198.87 ± 5.35	52.63 ± 3.15	Q
OSL-H1	5.3	4–11	2.09 ± 0.06	9.94 ± 0.26	2.39 ± 0.02	11	3.85 ± 0.18	255.50 ± 7.13	66.44 ± 3.65	Q
OSL-H14	6.2	4–11	2.33 ± 0.09	12.2 ± 0.52	2.37 ± 0.02	10	4.14 ± 0.22	279.67 ± 10.67	67.61 ± 4.47	Q
OSL-H15	7.1	4–11	2.23 ± 0.11	11.4 ± 0.33	2.32 ± 0.01	10	3.98 ± 0.21	351.35 ± 9.95	88.32 ± 5.23	Q
OSL-H17	9.6	4–11	2.29 ± 0.08	11.5 ± 0.16	2.5 ± 0.01	10	4.18 ± 0.2	451.54 ± 13.44	107.95 ± 6.11	F
OSL-H18	10.6	4–11	2.29 ± 0.08	11.5 ± 0.16	2.5 ± 0.01	10	4.18 ± 0.2	474.88 ± 14.78	113.71 ± 6.53	F
OSL-HH-54	15.7	63–90	2.93 ± 0.8	12.5 ± 0.3	2.28 ± 0.08	17	3.47 ± 0.2	465.60 ± 14.90	134.20 ± 6.5	F
OSL-HH-67	25.4	63–90	2.40 ± 0.68	12.8 ± 0.3	2.31 ± 0.08	14	3.52 ± 0.2	532.30 ± 30.60	151.40 ± 13.8	F

(Note: Q represents the quartz OSL age; F = represents the feldspar OSL age)

De of the quartz grains and K-feldspar grains using an automated Risø TL/OSL-DA-20C/D reader, which was equipped with a  $^{90}\text{Sr}/^{90}\text{Y}$  beta source. Additionally, the 32–125 μm quartz grains were extracted and etched in a dark room with HF under red light for ESR dating using Ti–Li center methods. Details for the OSL and ESR dating are shown in the Supplementary Text S1 and S2, respectively.

### 3. Results

#### 3.1. Magnetic susceptibility characteristics

The low-frequency magnetic susceptibility ( $\chi_{lf}$ ) of surface sediments ranges from  $5.93 \times 10^{-8}$  to  $661.44 \times 10^{-8} \text{ m}^3 \cdot \text{kg}^{-1}$ , with a mean value of  $89.13 \times 10^{-8} \text{ m}^3 \cdot \text{kg}^{-1}$ . The high-frequency magnetic susceptibility ( $\chi_{hf}$ ) varies between  $5.45 \times 10^{-8}$  and  $128.33 \times 10^{-8} \text{ m}^3 \cdot \text{kg}^{-1}$ , averaging  $28.95 \times 10^{-8} \text{ m}^3 \cdot \text{kg}^{-1}$ . The frequency-dependent magnetic susceptibility ( $\chi_{fd}$ ) ranges from 0.14 % to 17.32 %, with a mean of 3.11 %.

In the HS section,  $\chi_{lf}$  exhibits an overall range of  $6.72 \times 10^{-8}$  to  $46.10 \times 10^{-8} \text{ m}^3 \cdot \text{kg}^{-1}$ , averaging  $29.28 \times 10^{-8} \text{ m}^3 \cdot \text{kg}^{-1}$ , while  $\chi_{hf}$  ranges from  $6.27 \times 10^{-8}$  to  $45.17 \times 10^{-8} \text{ m}^3 \cdot \text{kg}^{-1}$ , with a mean of  $28.38 \times 10^{-8} \text{ m}^3 \cdot \text{kg}^{-1}$ . Both parameters show higher values in loess layers and lower values in paleosol layers. The lowest  $\chi_{lf}$  value occurs in paleosol layer S2S1, gradually increasing upward until a sharp decline at the middle part of L1S1 (4.9–5.15 m), where a pronounced low peak is observed. The  $\chi_{lf}$  values of loess layers remain relatively stable, averaging  $34.93 \times 10^{-8} \text{ m}^3 \cdot \text{kg}^{-1}$ , with a slightly higher value at the base of L2L2. The  $\chi_{fd}$ % in the HS section ranges from 0 to 0.26 %, with a mean of 0.03 %, displaying high-frequency variability without a clear correlation with loess or paleosol layers.

#### 3.2. DRS characteristics

The relative content of goethite (Gt) in the potential source area's surface sediments ranges from 0.04 % to 0.14 %, with a mean value of 0.08 %, while hematite (Hm) ranges from 0.05 % to 0.2 %, averaging 0.12 %. The two minerals exhibit a weak positive correlation ( $R^2 = 0.31$ ; Supplementary Fig. S1b) but show an extremely weak relationship with  $\chi_{lf}$  ( $R^2 = 0.08$  and 0.03, respectively; Supplementary Fig. S1b).

In the HS section samples, the relative content of goethite (Gt) ranges from 0.032 % to 0.143 %, with an average of 0.094 %, while hematite (Hm) content ranges from 0.053 % to 0.185 %, averaging 0.128 %. These two minerals are strongly positively correlated ( $R^2 = 0.87$ ) and exhibit co-varying trends with  $\chi_{lf}$  ( $R^2 = 0.54$  and 0.35, respectively; Supplementary Fig. S1a). The weak correlation between hematite (Hm) and goethite (Gt) in the source region can be attributed to distinct influences from differences in parent rocks and climatic conditions (Balsam et al., 2004; Ji et al., 2004). In contrast, the strong correlation observed in the depositional area indicates a significant influence from pedogenic processes (Ji et al., 2007). Specifically, the alternating wet and dry conditions during soil formation promote cyclical oxidation and reductive dissolution, facilitating the mutual transformation between hematite and goethite (Wang et al., 2012). Consequently, the Hm/Gt ratio no longer reflects the source-area climate but rather serves as an indicator of variations in soil moisture during pedogenesis (Ji et al., 2007). Both minerals display higher concentrations in loess layers compared to paleosol layers, with Hm always exceeding Gt in the latter. Through the paleosol sequence (S2S1 to S1S1), the abundances of both Hm and Gt show progressive decreases upward. However, in contrast to  $\chi_{lf}$  which reaches its minimum in the middle of L1S1, the lowest values of Hm and Gt occur at the uppermost part of L1S1. Within loess layers

**Table 2**

ESR Dating Results of the HS loess-paleosol section.

Sample No.	Depth (m)	Grain size (μm)	U (ppm)	Th (ppm)	K <sub>2</sub> O (%)	Water content(%)	Dose rate (Gy/ka)	Cosmic dose rate (Gy/ka)	Total dose rate (Gy/ka)	Equivalent dose (Gy)	Age (ka)
HH-ESR-43	21.75	32–125	2.41 ± 0.343	11.2 ± 0.025	2.53 ± 0.003	10	3.393	0.018	3.411	552 ± 62	162 ± 18
HH-ESR-52	24.45	32–125	2.56 ± 0.005	10.8 ± 0.008	2.72 ± 0.002	10	3.561	0.015	3.576	615 ± 60	172 ± 17

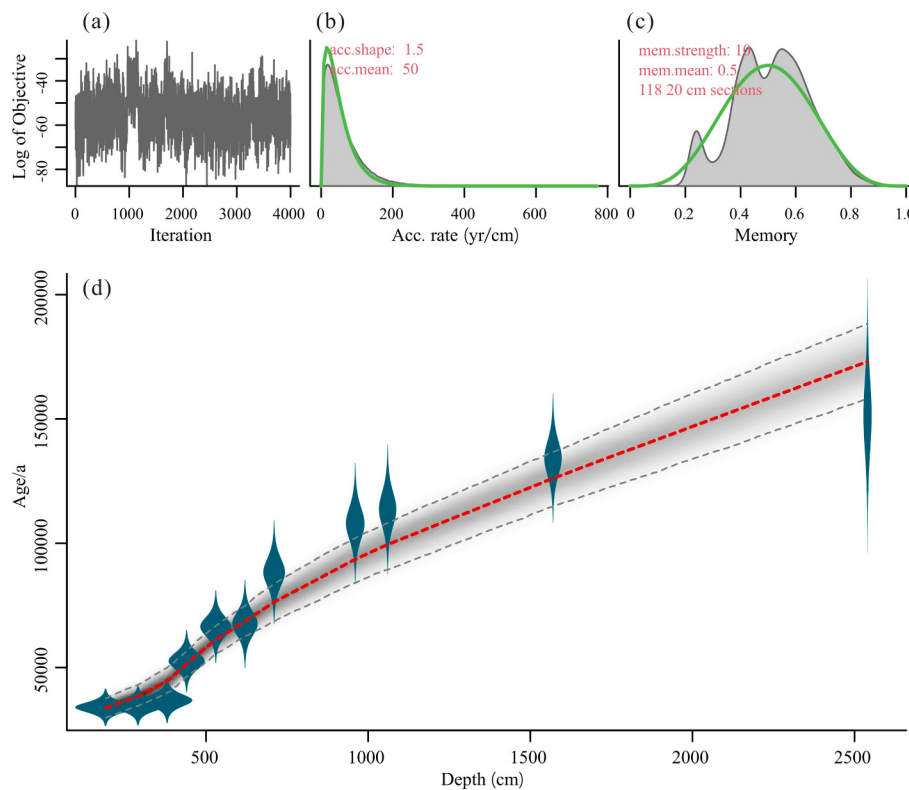


**Fig. 4.** The Bacon age-depth model for the HS loess-paleosol section (Blaauw and Christen, 2011; Blaauw et al., 2018). (a) The number of Markov Chain Monte Carlo (MCMC) iterations used to produce the gray-scale graphs. (b) The prior (green) and posterior (gray) distributions of precipitate accumulation rates. (c) The prior (green) and posterior (gray) distributions of memory, indicating the dependence of precipitate accumulation rates between successive depths. (d) Calibrated OSL ages (dark green, with  $2\sigma$  error) are plotted alongside the age-depth model. The dark gray shading represents the most probable calendar ages, while gray stippled lines denote the 95 % confidence intervals. The red curve shows the best model based on the weighted mean age for each depth. (For interpretation of the references to colour in this figure legend, the reader is referred to the web version of this article.)

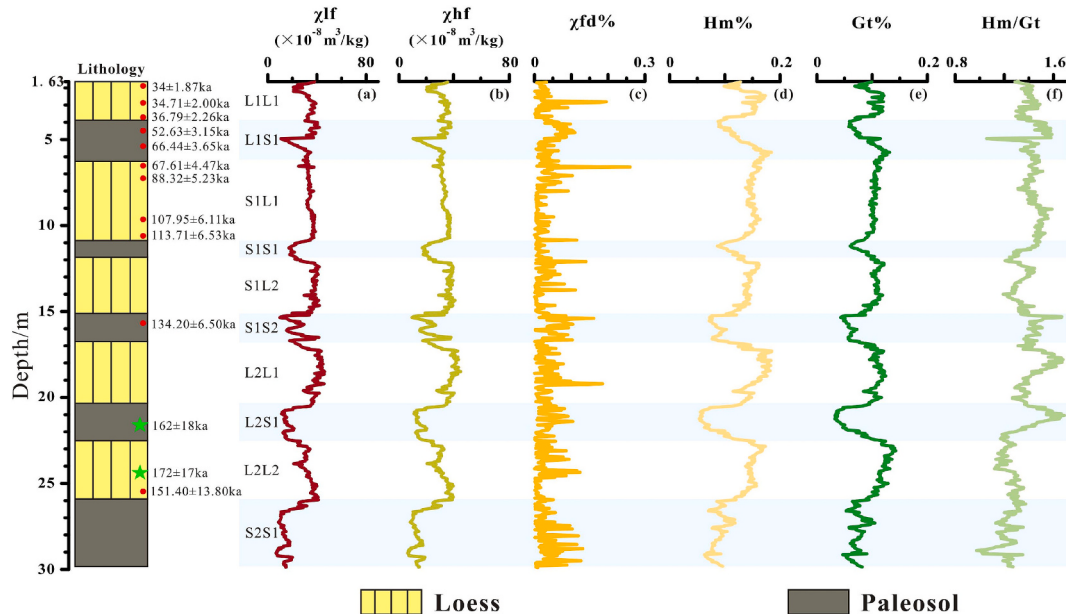


**Fig. 5.** Comprehensive profile of the HS loess-paleosol section including lithology, (a) low-frequency magnetic susceptibility, (b) high-frequency magnetic susceptibility, (c) frequency-dependent magnetic susceptibility, (d) hematite%, (e) goethite%, (f) hematite/ goethite. The red dots and green five-pointed stars on the right side of the lithology column represent the sampling location and dating results of OSL and ESR, respectively. The shaded areas in the figure represent the L1S1, S1S1, S1S2, L2S1, L2L2, S2S1 paleosol layers. (For interpretation of the references to colour in this figure legend, the reader is referred to the web version of this article.)

(L2L2–L1L1), the concentrations of Hm and Gt remain relatively stable, with mean abundances between 0.10 % and 0.16 %. The section-wide Hm/Gt ratio varies from 0.974 to 1.689 (mean = 1.368), with peak ratios observed in L2L1, L2S1, S1S2, and the top of L1S1. By contrast, S2S1 and L2L2 exhibit markedly low ratios. Notably, the Hm/Gt ratio minimum in the middle of L1S1 aligns with the  $\chi_{lf}$  nadir.

### 3.3. Chronology of the Harbin Loess

The OSL and ESR dating results for the HS loess-paleosol section are shown in Table 1 and Table 2. The Bacon age-depth model indicates the ~195 ka basal age for the loess-paleosol sequence (Fig. 4). ESR dating is used only to verify the accuracy of the age framework in considering the error effect (Zeng et al., 2017). The measured ESR ages are both <200 ka, indicating that the age framework established in this study is accurate and it can be used for subsequent paleoclimatic analysis.

## 4. Discussions

### 4.1. Characteristics of magnetic susceptibility and their paleoclimatic significance

Magnetic susceptibility is a measure of how easily sediments can be magnetized in a magnetic field, providing reliable magnetic evidence for inferring the palaeoclimatic environment in which sediments were formed (Jordanova and Jordanova, 2021; Liu et al., 2017). While frequency-dependent magnetic susceptibility ( $\chi_{fd}\%$ ) has been widely recognized as an indicator of pedogenic intensity (Chen et al., 2018), the surface sediments from potential source areas of the Harbin loess exhibit particularly low  $\chi_{fd}\%$  values (mean: 3.11 %). Notably, the loess profile samples show near-zero  $\chi_{fd}\%$  values (mean: 0.038 %; Fig. 5c), indicating that the detrital materials from the source region initially contain a limited quantity of superparamagnetic (SP) particles. The near absence of SP particles in the loess-paleosol layers during pedogenesis may be attributed to either post-depositional redox conditions (Liu et al., 2007a, 2007b) or weathering intensity (Kalm et al., 1996). The significantly lower  $\chi_{fd}\%$  values observed in the Harbin loess-paleosol sequence, in comparison to those in the potential dust source regions, indicate that not only was there no neoformation of ultrafine-grained magnetic minerals during pedogenesis, but also that the detrital ferrimagnetic minerals derived from the dust source regions were dissolved under reducing pedogenic conditions. Consequently,  $\chi_{fd}\%$  has lost its climatic significance in this region (Hou, 2016).

In contrast to  $\chi_{fd}\%$ , the  $\chi_{lf}$  values in the HS section exhibit higher magnitudes in loess layers and lower values in paleosol layers. The paleosol S1S2 in the northern Iranian loess-paleosol sequences (Najafi et al., 2019; Guo et al., 2012) and the paleosol layers in high-latitude Northern Hemisphere locations, such as Alaska and Siberia (Liu et al., 2020; Liu et al., 2007a; Liu et al., 2008; Liu et al., 2008b), show parallels to this magnetic attenuation event. Increased precipitation (Balsam et al., 2011; Zhao et al., 2008), pedogenic redox conditions (Liu et al., 2007a, 2007b), and changes in wind intensity (Begét et al., 1990; Chlachula, 2003) may all be linked to the observed magnetic reduction.

The paleosols in the HS section are rich in humus and predominantly exhibit gray-brown to gray-black coloration, as illustrated in the outcrop sections (Fig. 5). These soils developed through a distinctive meadow process (Wu, 1959) and primarily form in regions where permafrost is present (Cui et al., 2003). During relatively warm and humid periods, although the active permafrost layer melts, the meltwater cannot percolate downward due to the blocking of permafrost layer, and instead migrates from the lower part with a higher water potential to the upper part (He et al., 2023; Li et al., 2021; Wang, 2022). The soil water content gradually increases with the increase in freezing-thaw cycles (Xiao et al., 2020). Ferromagnetic minerals in soil are reduced and decomposed under long-term high humidity and waterlogged environments (Liu et al., 2007b), and high-valent iron is reduced to low-valent iron, which

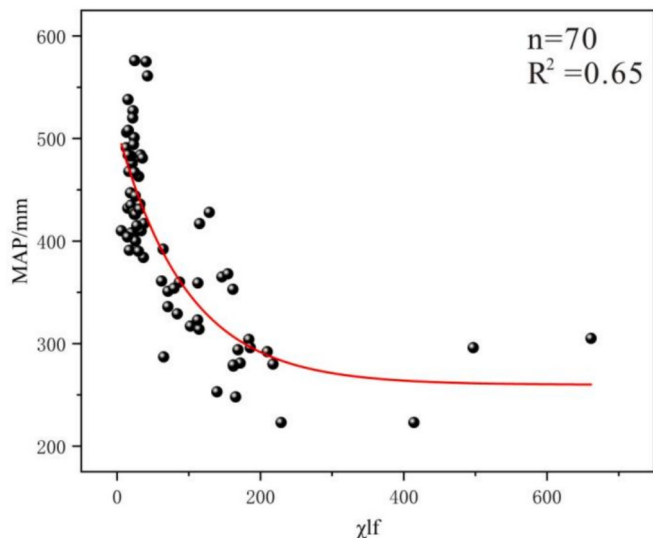
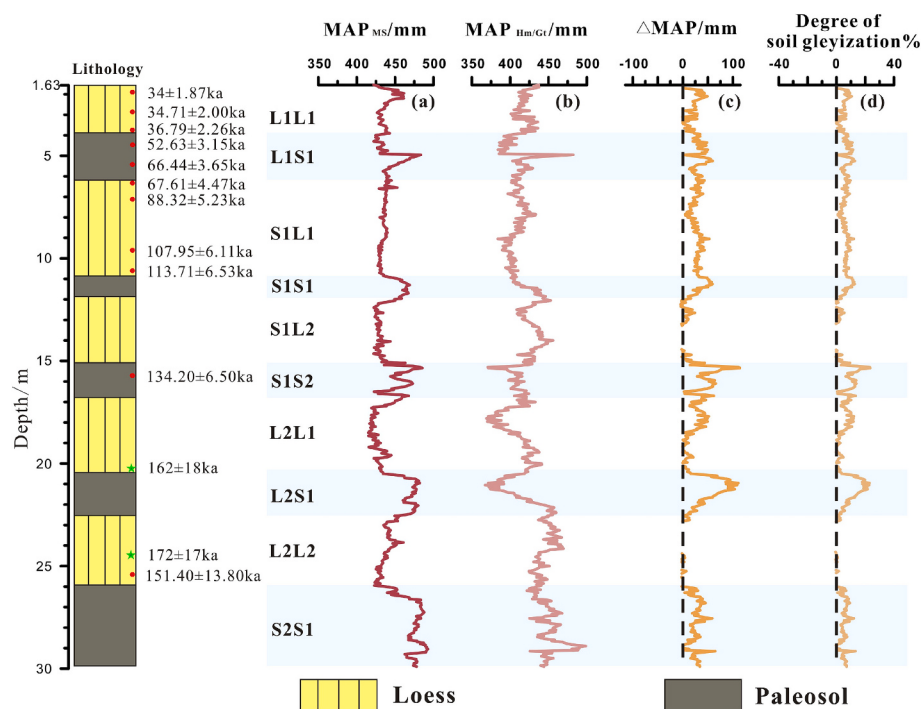


Fig. 6. Fitting curve of the topsoil magnetic susceptibility and MAP in the potential dust source areas.

migrates and leaches downward or laterally with soil solution. When the soil is continuously saturated with water, the free iron in the soil is continuously reduced, resulting in soil decolorization to form a white layer (e.g., bleaching layer, Brinkman, 1970; Brinkman, 1977; Lü and Xu, 1991; Gao et al., 1988; Lü and Xu, 1993), as seen in the paleosol L1S1 (Fig. 2A). Under reduced conditions, strong magnetic minerals can be transformed into weak magnetic ones (Yu, 1979; Yu et al., 1981), resulting in white precipitations observed in the paleosol layers L2S1 and S2S1 (Fig. 2C). The stronger the gleyization (reduction) intensity in soils and the lower the magnetic susceptibility values, so the magnetic susceptibility values of the S2S1 layer are lower than those of the L2S1 layer. The magnetic susceptibility values of the S1S2 layer show a gradual transition from oxidizing conditions at the base to reducing conditions upward, with slightly higher (lower) values at the bottom (top) (Fig. 5). Combined with the lithology of the profile, the lower magnetic susceptibility zone at the top corresponds to light to dark gray paleosols, indicating a reduced environment with higher soil moisture during deposition. However, the higher magnetic susceptibility zone at the bottom, with rust-colored paleosol and well-developed muddy gravels (Figs. 2B, D) in response to a dry, well-drained oxidizing environment, suggesting that ferric iron can be reduced to ferrous iron in a humid soil environment (Peng et al., 2021).

In the Harbin region, precipitation is primarily influenced by the East Asian Summer Monsoon (Sun et al., 2017). The relatively higher rainfall and elevated temperatures during interglacial periods, as compared to loess deposition phases, triggered permafrost thawing. This resulted in an increase in soil moisture, often to excessive levels, thereby promoting gleyization processes (Zhao et al., 2008; Liu et al., 2007; Guo et al., 2012). In this scenario, the limited content of strongly magnetic maghemite grains was progressively transformed into weakly magnetic minerals, such as hematite and limonite (Chlachula, 2003; Liu et al., 2007a; Zhang et al., 2021), ultimately resulting in a low magnetic susceptibility value.

To quantitatively assess the relationship between magnetic susceptibility ( $\chi$ ) and soil moisture content, we conducted a correlation analysis of the low-frequency magnetic susceptibility of the topsoil in the potential dust source areas of the Harbin loess with the mean annual precipitation (MAP). Based on this, the regression equation with the highest level of statistical significance and the largest determination coefficient ( $R^2 = 0.65, p < 0.01$ ) is selected to establish the relationship between the low-frequency susceptibility and MAP (Fig. 6):  $MAP = 259.82135 + 249.39084e^{-\frac{\chi_{lf}}{97.16212}}$ . The nonlinear model for magnetic



**Fig. 7.** Precipitation reconstructed from the magnetic susceptibility (a), precipitation reconstructed from Hm/Gt ratio (b), difference between MAP<sub>MS</sub> and MAP<sub>Hm/Gt</sub> (c), degree of soil gleyization ( $\Delta$ MAP/MAP<sub>MS</sub> × 100 %) (d) in the HS loess-paleosol section. The black dotted lines represent the baselines. The red dots and green five-pointed stars on the right side of the lithology column represent the sampling location and dating results of OSL and ESR, respectively. The shaded areas in the figure represent the L1S1, S1S1, S1S2, L2S1, S2S1 paleosol layers. (For interpretation of the references to colour in this figure legend, the reader is referred to the web version of this article.)

susceptibility versus MAP demonstrates a correlation coefficient ( $r$ ) of  $-0.816$ , with  $R^2 = 0.661$ , adjusted  $R^2 = 0.650$ , and  $p < 0.01$ . The discrepancy between the adjusted and original  $R^2$  values is less than 0.05, indicating a moderate explanatory power of the model. Furthermore, a comparison of the model's root mean square error (RMSE) with the observed mean MAP yielded a relative error of 13 %, which is below the 30 % acceptability threshold, suggesting acceptable prediction accuracy. Diagnostic analyses revealed that the residual frequency distribution closely approximates a normal distribution (Supplementary Fig. S3a), and residual scatterplots displayed no distinct linear trend or clustering patterns (Supplementary Fig. S3b). These findings support the conclusion that the model meets the linearity assumption and exhibits well-behaved residual randomness. Thus, the MAP<sub>MS</sub> during the deposition of the HS loess-paleosol sequence can be derived by incorporating the  $\chi_{lf}$  values of the HS section into the aforementioned equation. The magnetic attenuation observed in the paleosols of the HS section is attributed to increased soil moisture, which is jointly influenced by precipitation and reduction processes. Consequently, the calculated paleoprecipitation values (MAP<sub>MS</sub>) incorporate all soil water sources, including atmospheric precipitation and meltwater (Fig. 7a). In terms of vertical variation, the reconstruction reveals that the paleosol layers exhibit significantly higher MAP<sub>MS</sub> values than the loess layers. For the loess units (L2L2-L1L1), the MAP<sub>MS</sub> values remain relatively constant (427.75–438.83 mm). In contrast, the paleosols exhibit progressive changes: the S2S1 layer exhibits the highest mean MAP<sub>MS</sub> value of 474.64 mm, with peak values gradually decreasing upward. The MAP<sub>MS</sub> value in the L1S1 layer is nearly equivalent to that of the loess layers; however, within its middle section (4.9–5.15 m), the MAP<sub>MS</sub> value experiences a sharp increase, reaching a peak of 467.93 mm. Given that MAP<sub>MS</sub> values are primarily influenced by atmospheric precipitation and freeze-thaw meltwater, the higher MAP<sub>MS</sub> values may indicate an increase in rainfall, elevated temperatures (resulting in greater freeze-thaw meltwater), or a combination of both factors.

#### 4.2. The characteristics of goethite and hematite and their paleoclimate significance

Hematite and goethite in loess-paleosols are highly sensitive to hydrothermal alterations (Hu and Liu, 2014), making them valuable indicators of glacial-interglacial cycles and useful for reconstructing paleoprecipitation and paleo-temperature (Ji et al., 2004; Heller and Liu, 1984, 1986; George et al., 1988; Deng et al., 2006). The test results indicate that the relative contents of hematite (Hm) and goethite (Gt) in the paleosol layer of the HS section are significantly lower than those in the loess layer (Figs. 5d, e), exhibiting magnetic reduction similar to  $\chi_{lf}$ . Compared with the relative Hm and Gt contents of the surface sediments from the potential source areas, the loess layer in the HS section, with average values of 0.148 % and 0.108 %, respectively, aligns well with the surface deposits. This finding suggests that iron oxide minerals underwent minimal transformation or loss during the transport or weathering of eolian loess. Consequently, the observed decrease in Hm and Gt contents in the paleosol layer is likely attributed to subsequent pedogenic processes.

The formation of paleosols is governed by dual control from hydrological and thermal conditions, influenced by both the atmosphere and the soil matrix itself (Yang et al., 2024). The Hm/Gt ratio in the HS section demonstrates no systematic variation correlated with loess-paleosol stratigraphy. Notably, specific paleosol horizons (particularly S2S1, S1S1, and the mid-section of L1S1) exhibit lower Hm/Gt ratios compared to adjacent loess units (Fig. 5f). Magnetic susceptibility data suggest that paleosol formation in Harbin was characterized by significant gleyization, driven by the combined influences of meteoric precipitation and seasonal freeze-thaw cycles. This pedogenic process enhanced soil moisture, thereby facilitating the precipitation of secondary goethite (Hyland et al., 2015; Peppe et al., 2009) and consequently leading to a decrease in the Hm/Gt ratio. In hydromorphic reducing environments with inadequate drainage, periodic stagnant water environment further inhibited hematite formation (Hyland et al.,

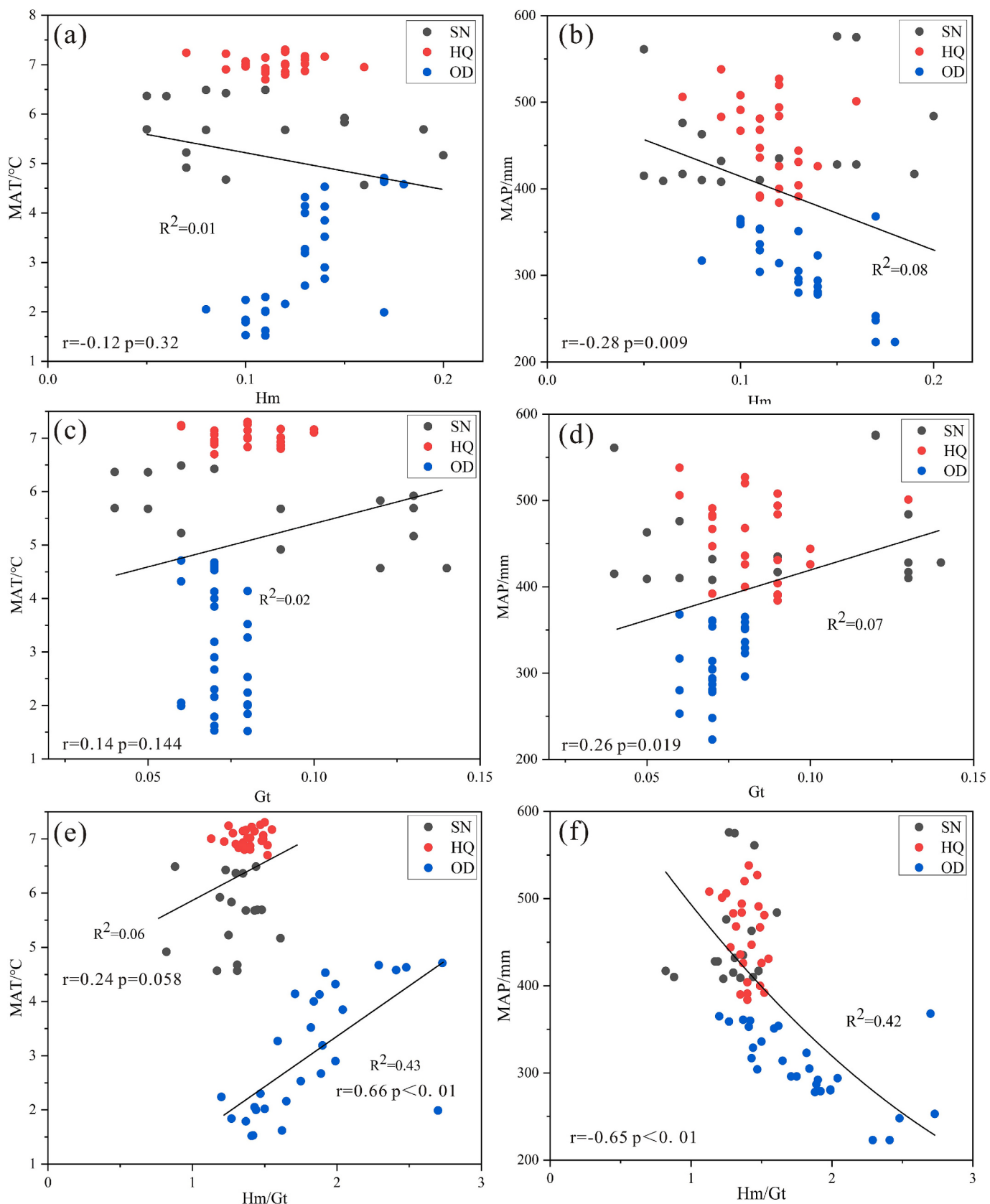


**Fig. 8.** Plots of Hm against MAT (a) and MAP (b), Gt against MAT (c) and MAP (d), Hm/Gt against MAT (e) and MAP (f) in the topsoil of the potential dust source areas. The meteorological data are derived from version 2.1 of the WorldClim dataset, available at [www.worldclim.org](http://www.worldclim.org), with a spatial resolution of 1 km $^2$  and covering the years 1970–2000. Ordinary Kriging interpolation was conducted on the sampling points using ArcGIS software to obtain the MAT and MAP.

2015; Torrent et al., 2010). Furthermore, organic matter can significantly influence the formation of iron oxides in soils. The paleosols in the HS profile are predominantly grayish-brown (Zhang et al., 2021). Although the exact organic matter content remains uncertain, the development of modern organic-rich black soils in this region suggests that the paleosols in the HS profile may also have contained a certain amount of organic matter. In poorly drained soils, organic matter enhances reducing conditions, which not only suppresses hematite formation (Schwertmann, 1971) but may also promote the dissolution of pre-existing hematite, ultimately preserving goethite (Fey, 1983). This process contributes to the observed low Hm/Gt ratios. In contrast, paleosol layers L2S1, S1S2, and the top of L1S1 exhibit significantly higher Hm/Gt ratios compared to adjacent loess layers, demonstrating the absolute dominance of hematite. This suggests that, in addition to the aforementioned pedogenic factors, temperature also plays a non-negligible role. Thermodynamic experiments indicate that higher temperatures favor the transformation of goethite to hematite (Gianella et al., 2010; Gualtieri and Venturelli, 1999), while arid environments, where evaporation exceeds precipitation, promote hematite formation (Zhu et al., 2022; Wu et al., 2018). Therefore, the variability in relative Hm and Gt contents and their ratios across different paleosol layers requires comprehensive evaluation from multiple perspectives, including temperature, precipitation, and soil reduction (gleyization) processes. Quantifying the response of these climatic proxies to environmental factors will enhance our understanding of magnetic mineral transformations during pedogenesis.

In this study, we established correlation models for Hm, Gt, and the Hm/Gt ratio with MAT and MAP. The result indicate that the relationships between the Hm or Gt and MAT or MAP are very low (Figs. 8a-8d). A plausible explanation for this observation is that these two individual indicators exhibit insufficient sensitivity to variations in temperature and precipitation. While Hm or Gt in certain potential dust source regions, such as Onqin Daga Sandy Land (OD) and Horqin Sandy Land (HQ), may exhibit positive or negative correlations with precipitation or temperature (Guo et al., 2024; Zhang et al., 2024), the overall correlation between these indices and climatic factors across larger areas remains weak. This is attributed to the influences of local climate, parent rock type, and the degree of weathering (Pineau et al., 2007; Trolard and Tardy, 1987; Wu et al., 2018), making it challenging to characterize regional changes in temperature or precipitation.

Notably, the Hm/Gt ratio exhibits a significant positive correlation with mean annual temperature(MAT) in the single sandy land, as illustrated in Fig. 8e, suggesting that temperature may be the primary factor influencing the formation of hematite. However, the dispersed distribution of the surface soil samples across all potential dust source areas hinders the establishment of a precise relationship model. In this region, temperature likely exerts an indirect influence on iron mineral transformation by accelerating permafrost thawing, which in turn increases soil moisture content. Furthermore, Fig. 8f reveals that the Hm/Gt ratio gradually declines with rising mean annual precipitation (MAP). This negative correlation has also been documented in the Huanxian and Yanchang sections of the Loess Plateau (Ji et al., 2004), as well as in the loess-paleosol sequences of Luochuan and Sanmenxia (Wang et al., 2016). The Hm/Gt ratio not only serves as a reliable proxy for precipitation variability but also effectively reflects the intensity variations of the East Asian Summer Monsoon (Jiao et al., 2023). Therefore, we established a quantitative relationship model between the Hm/Gt ratio and MAP (mean annual precipitation) for the surface sediments from the potential source regions:  $MAP = 28.56x^2 - 259.47x + 724.18$  ( $R^2 = 0.42$ ,  $p < 0.01$ ). The nonlinear model correlating the hematite-to-goethite ratio with MAP demonstrates a correlation coefficient ( $r$ ) of  $-0.659$ , with  $R^2 = 0.434$ , adjusted  $R^2 = 0.417$ , and  $p < 0.01$ . The difference between the adjusted and original  $R^2$  values is less than 0.05, indicating moderate explanatory power. A comparison of the model's RMSE to the observed mean MAP yields a relative error of 17 %, below the 30 % acceptability threshold, indicating acceptable prediction

accuracy. Diagnostic analysis reveals that the residual frequency distribution closely approximates a normal distribution (Supplementary Fig. 3S. c), and the residual scatter plot shows no discernible linear trend or clustering pattern (Supplementary Fig. 3S. d), supporting the conclusion that the model meets the linearity assumption and exhibits well-behaved residual randomness. The Hm/Gt-MAP model can be effectively utilized to reconstruct paleo-precipitation for each layer in the HS section, thereby producing vertically continuous precipitation changes based on the Hm/Gt ratio (Fig. 7b). The reconstruction results indicate that the S2S1 paleosol layer exhibits the highest mean  $MAP_{Hm/Gt}$  value of 450.01 mm, while the lowest peak of 367.47 mm occurs in the middle L2S1 layer. The S1S2 and S1S1 layers show slightly increased mean values of 408.05 mm and 422.66 mm, respectively. Notably, the mid-section of L1S1 (4.9–5.15 m depth) demonstrates a dramatic increase in  $MAP_{Hm/Gt}$ , reaching a maximum of 482.08 mm, followed by a sharp decrease to 395.09 mm upward. Overall, the  $MAP_{Hm/Gt}$  curve exhibits irregular variations across paleosol layers, revealing significant discrepancies with  $MAP_{MS}$ . This suggests that the impacts of atmospheric precipitation and freeze-thaw processes on the Hm/Gt ratio warrant critical reassessment.

During the development of paleosols in Harbin, stagnant water environment (Li et al., 2022) or reducing conditions (Li et al., 2019b) led to increased soil moisture, which results in significantly lower relative abundances of Hm and Gt in paleosols compared to loess layers. Consequently, these two parameters cannot directly indicate variations in monsoon precipitation. However, the Hm/Gt ratio can approximately eliminate the influence of freeze-thaw water, as evidenced by its fluctuating (rather than systematically lower) values in paleosols compared to loess—unlike the marked depletion observed in  $\chi_{lf}$ . This observation suggests that the impact of freeze-thaw water on the Hm/Gt ratio is minimal. Supporting evidence comes from ODP Site 1143 sediments, where terrigenous iron oxides (Hm and Gt) were found to retain monsoon-related signals unaffected by post-depositional redox processes (Zhang et al., 2007). Therefore, in this study, we use the Hm/Gt ratio to approximate monsoon precipitation, explicitly excluding non-atmospheric water sources such as freeze-thaw meltwater. We can calculate the difference between the two precipitation reconstruction methods ( $MAP_{MS} - MAP_{Hm/Gt}$ ), denoted as  $\Delta MAP$ , reflects the amount of non-atmospheric precipitation, including freeze-thaw water (Fig. 7c). Therefore, we propose that the degree of soil gleyization (i.e., degree of water stagnation) can be defined as: freeze-thaw water ( $\Delta MAP$ ) / soil water ( $MAP_{MS}$ )  $\times 100\%$ .

The estimation results indicate that the degree of soil gleyization has a significant correspondence with the loess and paleosol layers. Specifically, the loess exhibits a gleyization of essentially 0, indicating no gleyization, whereas the paleosols display varying degrees of gleyization (Fig. 7d). Among these, the paleosol S1S2 and L2S1 demonstrate the highest gleyization degrees, with mean values of 10.65 % and 11.44 %, respectively, followed by L1S1 and S1S1 (mean values of 7.49 % and 8.41 %, respectively), while S2S1 exhibits the lowest degree of gleyization (5.18 %) (Fig. 7d). In the mid-latitude permafrost region, the rising temperatures during interglacial periods lead to the melting of permafrost, with an increase in freeze-thaw water contributing to a greater degree of soil gleyization. Consequently, variations in paleotemperature can be inferred from the gleyization degrees of different paleosol layers.

Considering the vertical variation characteristics of reconstructed precipitation (Fig. 7), it can be inferred that during the deposition of S2S1, the Hm/Gt ratio exhibits an increasing trend in atmospheric precipitation, with a mean value of 450 mm, while the soil moisture content remains elevated, averaging 474.64 mm. The minimal disparity between these values suggests limited meltwater input, gradual permafrost degradation, and consequently, prevailing cold climatic conditions, suggesting a robust EASM and an overall cold and humid climate. Beginning with L2S1, there was a notable increase in the degree of soil gleyization, which signifies a warming climate and extensive

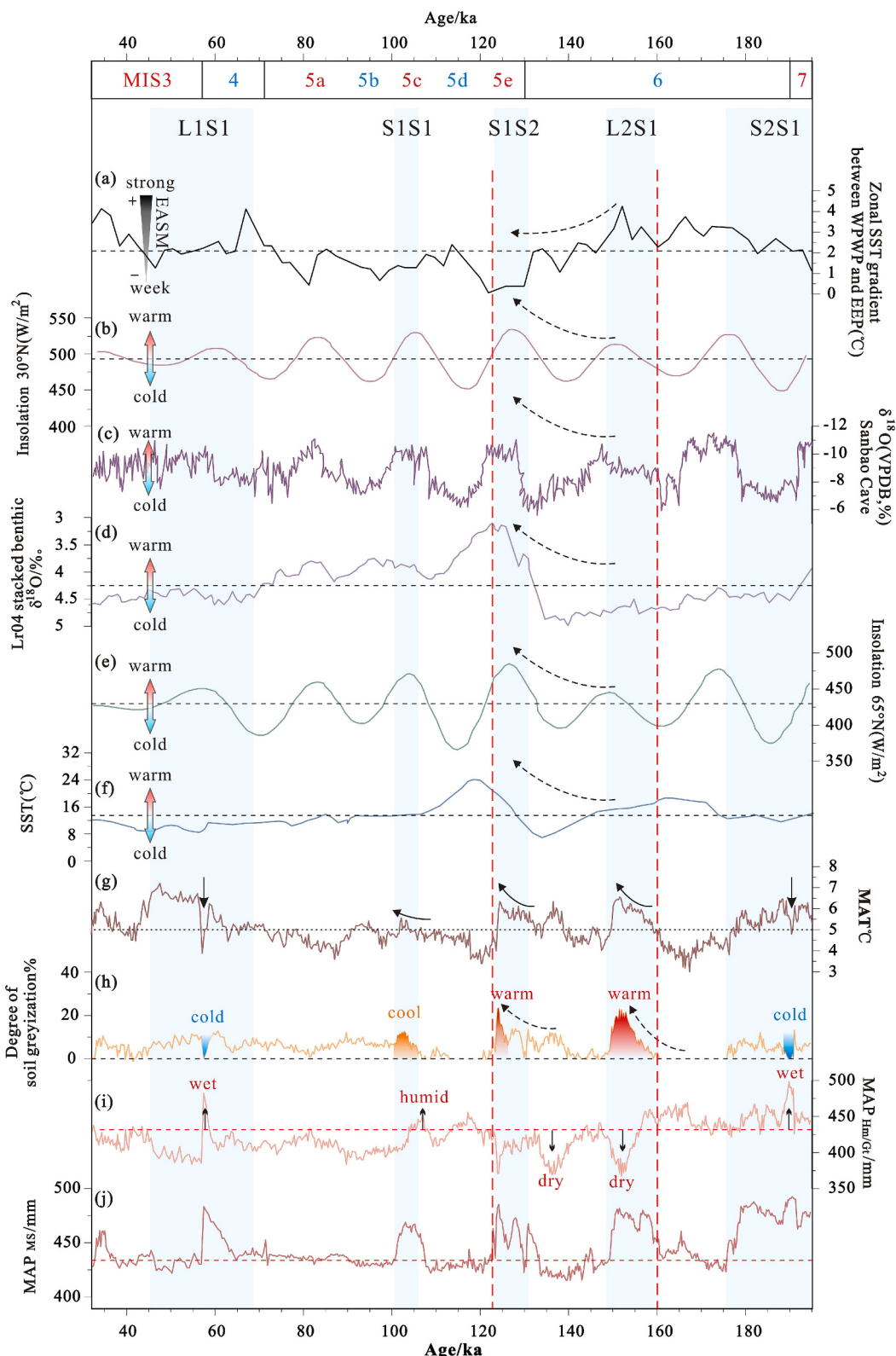


**Fig. 9.** Comparison among the proxy records from the HS loess-paleosol sequence with (a) Zonal SST gradient between WPWP and EEP (Zhang et al., 2023), (b) Northern Hemisphere summer solar radiation at 30° N (June) (Berger, 1978), (c) Sanbao Cave stalagmite  $\delta^{18}\text{O}$  records (Cheng et al., 2016), (d)  $\delta^{18}\text{O}$  of LR04 stack (Lisiecki and Raymo, 2005), (e) Northern Hemisphere summer solar radiation at 65° N (July–September) (Laskar et al., 2004), (f) sea surface temperature (SST) in the Northwest Pacific Ocean (Matsuzaki et al., 2014), (g) Paleotemperature reconstruction in the Harbin loess (Zhou et al., 2025), (h) degree of paleosol gleyization in the Harbin loess, (i) precipitation reconstructed from Hm/Gt ratio, (j) precipitation reconstructed from the magnetic susceptibility. The red vertical dotted lines represent the boundaries between the three climate evolution stages of the Songnen Plain since 195 ka. The red horizontal dotted lines represent the “precipitation threshold”, the black dotted lines represents the mean values of the proxies. The black dotted arrow represents the change trend of each index. The blue shading represents the paleosol layers in the HS section. (For interpretation of the references to colour in this figure legend, the reader is referred to the web version of this article.)

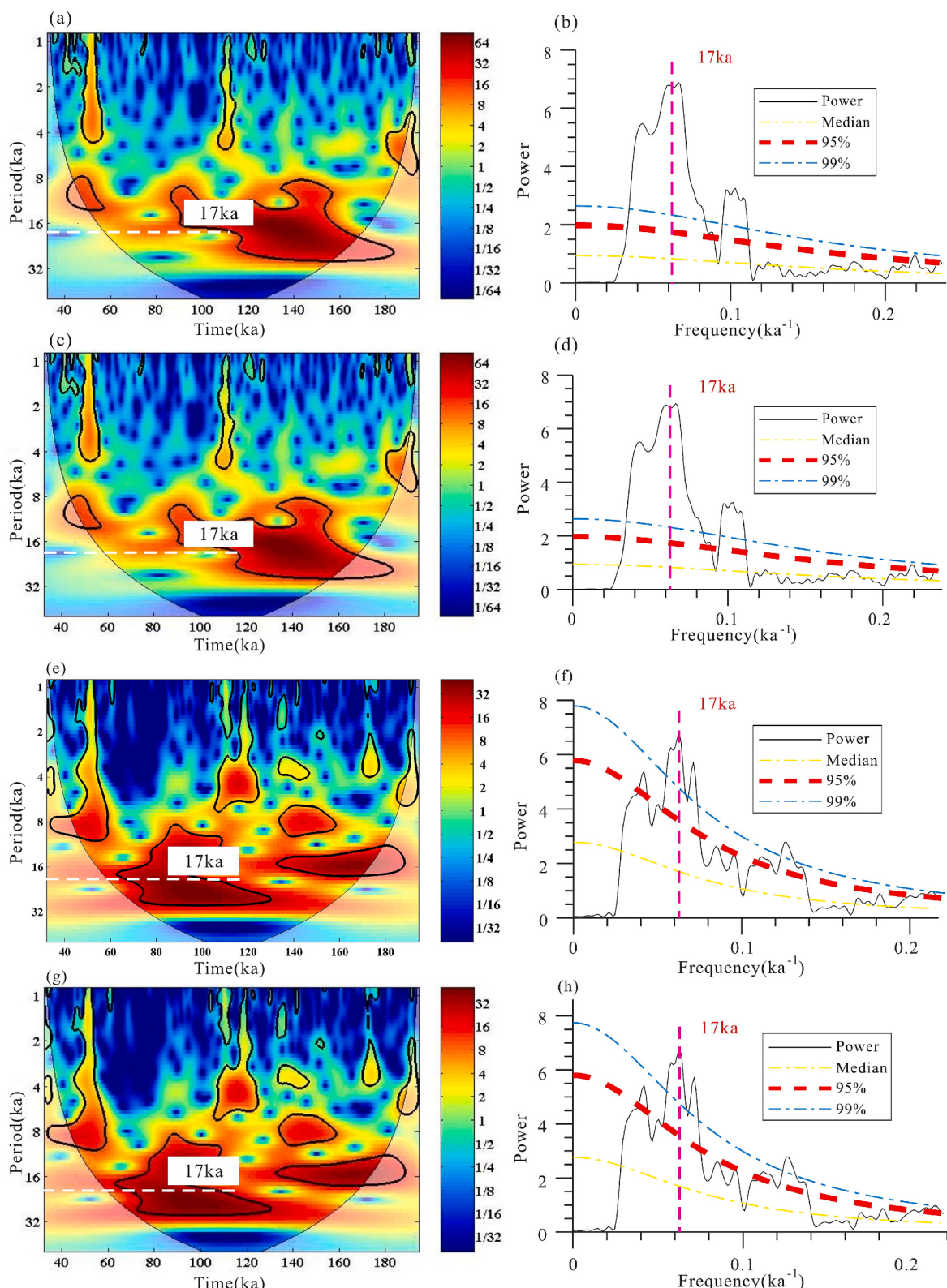


**Fig. 10.** Wavelet power spectrum and spectral analysis of magnetic susceptibility (a), precipitation reconstructed from magnetic susceptibility (c), Hm/Gt ratio (e), precipitation reconstructed from Hm/Gt ratio (h) in the HS loess-paleosol section. Wavelet power spectrum was processed using Matlab software (Paterson and Heslop, 2015; Wang et al., 2018). Solid black contour identifies the region where the spectral power meets the 95 % significance level, and the white dashed line represents the main period of precession (~17ka). Spectrum analysis was conducted using the Acycle time series analysis software (Li et al., 2019a), where yellow, red and blue represent the theoretical median, 95 % and 99 % false alarm levels, respectively. Purple dotted lines show significant peaks at a period of 17 ka. (For interpretation of the references to colour in this figure legend, the reader is referred to the web version of this article.)

thawing of permafrost, resulting in an increase in surface freeze-thaw water. Concurrently, atmospheric precipitation experienced a significant decline, with a mean value of 414.18 mm, and soil moisture showed a decreasing trend. These findings imply a weakening of the EASM and an overall warm and dry climatic environment in the study area. While atmospheric precipitation remains the primary source of soil water, the contribution of freeze-thaw water to the surface is significant and should not be overlooked. The reduction and decomposition of ferromagnetic minerals result in a marked decrease in the low-frequency magnetic susceptibility values (Liu et al., 2007). By the time of S1S1 deposition, the degree of soil gleyization continued to decline, indicating a transition to a cooler climate characterized by a slower rate of permafrost thawing. Despite this, both soil moisture and atmospheric precipitation exhibited an increase, suggesting the persistence of a cool and humid climate until the L1S1 period. Both soil water and atmospheric precipitation experienced a significant decline during L1S1, approaching the levels observed in the S1S2 and L2S1, which signifies a shift to a cool and dry climate. Additionally, a 0.25 m-thick grayish-white clay layer, located in the middle part of L1S1 (Fig. 2A), exhibits abnormally low  $\chi_{lf}$  values (close to zero), and climatic characteristics comparable to those of the S2S1 layer, suggesting cold and wet conditions. These interpretations are further supported by a notably low precipitation difference and a significant reduction in the intensity of soil gleyization. This evidence indicates that during the deposition of this grayish-white clay layer, there was a drop in temperature and an enhancement in the activity of the EASM, and the combined effects of East Asian Summer Monsoon precipitation and freeze-thaw water accelerated the rapid decomposition of organic matter and ferromagnetic minerals in the soil (Huang et al., 2018; Long et al., 2011, 2016; Lu, 1999; Schwertmann, 1971).

In summary, the process of soil gleyization in the Harbin area has resulted in a decoupling of the  $\chi_{lf}$ , Hm, Gt, and Hm/Gt ratio from the pedogenic processes. Nevertheless, the precipitation of the MS and Hm/Gt, reconstructed from the surface sediments in the potential dust source areas, can be utilized to quantitatively estimate the degree of paleosol gleyization. This approach facilitates the reconstruction of paleoclimate and the analysis of the intensity of the EASM activity.

#### 4.3. Climatic patterns and Mechanisms in the Songnen Plain since the late Middle Pleistocene

##### 4.3.1. Paleoclimate evolution process

Based on the quantitative estimations of paleoprecipitation and paleosol gleyization established by the MS, Hm/Gt, and MAP models, the paleoclimate evolution of the Songnen Plain since the late Middle Pleistocene can be divided into three distinct stages.

(1) The first stage, 195–160 ka. Under cold and wet climatic conditions, as indicated by the reconstructed paleotemperatures showing a decreasing trend (Fig. 9g), the permafrost remained essentially unthawed, and the degree of soil gleyization was low. However, the strong EASM introduced abundant atmospheric precipitation, resulting in high soil humidity. Research on grain size, total organic carbon (TOC) and Sr–Nd isotopic indicators in the Harbin loess has demonstrated that since 180 ka, there has been an increase in monsoon precipitation (Wu et al., 2021; Zhao et al., 2022), facilitating a transition from arid to humid conditions in the Songnen Plain.

(2) The second stage, 160–123 ka. The period was characterized by a warming climate, as indicated by the reconstructed paleotemperatures (Fig. 9g), leading to significant permafrost melting and an increase in soil gleyization. Simultaneously, there was a marked weakening of the EASM, leading to a substantial decrease in atmospheric precipitation. This declining trend in precipitation was observed in other regions of the Northern Hemisphere (Beck et al., 2018; Sun et al., 2019). Collectively, the study area experienced a warm and dry climate. This stage represents a critical transition from the Marine Isotope Stage (MIS) 6 to MIS 5, with the paleoclimatic reconstructions derived from the sediment and

pollen of the LS01 core in the Yinchuan Basin also indicating a warming trend (Xu et al., 2021, 2023).

(3) The third stage, 123–50 ka. The region experienced a cooling climate, marked by a slowdown in permafrost melting. Monsoon precipitation became the primary source of soil moisture; however, it was significantly lower compared to the first stage, only slightly exceeding that of the second stage, which indicates a persistently weak EASM. The study area was characterized by a predominantly cold and arid climate, interspersed with episodic warm and humid fluctuations. Nevertheless, during this period, the EASM intensified in two episodes: from 105 to 100 ka (S1S1), roughly corresponding to MIS 5c, and from 65 to 55 ka (lower-middle L1S1), during the transition from MIS 4 to MIS 3. From 105 to 100 ka, this period was characterized by increased temperatures. This trend aligns with the reconstructed paleotemperatures (Fig. 9g), indicating enhanced soil gleyization and an increase in monsoon precipitation. From 65 to 55 ka, the climatic conditions during this phase were consistent with those of the earlier stage, suggesting a cold interval (Fig. 9g). The palynological assemblages in the Songnen Plain (Xia and Wang, 1987), grain size and magnetic susceptibility studies of the Bei'an loess (Song et al., 2024) and research on the black soil in Baiquan (Shao et al., 2024) also indicate that since the Late Pleistocene, the Songnen Plain has generally experienced a cold and dry climate, punctuated by transitions to cold-humid and warm-cool conditions (Xia and Wang, 1987).

##### 4.3.2. The evolutionary mechanisms of the EASM in the Songnen Plain

Since the Middle Pleistocene Transition (MPT) (Strani et al., 2019; Lu, 2015), the changes in the orbital period of the EASM and its driving mechanism have become focus issues in the field of paleoclimatology (Yi et al., 2018; Sun et al., 2022; Ren et al., 2025; Caley et al., 2014). The Songnen Plain, situated at the northern margin of the EASM in the middle latitudes of the northern Hemisphere, serves as a critical area where the ocean circulation interacts with the climate system across high and low latitudes (Wu et al., 2023). The continuous loess-paleosol sequence in this region provide a valuable record of the EASM since the end of the Middle Pleistocene.

The comparison of the reconstructed precipitation record with the global climate record indicates that from 195 to 132 ka, there was a decrease in the intensity of summer insolation at 65°N, Arctic ice volume, and sea surface temperatures (SST) in the Northwest Pacific, followed by a sharp increase in the late Pleistocene (~123 ka) (Figs. 9d, e, f). These changes had a profound impact on the EASM precipitation. Influenced by the northward shift of the northern boundary of the EASM during MIS 7 and the changes in monsoon intensity, precipitation increased in northern China (Fig. 9i) while decreased in southern China (Wang and Zhang, 2020). As solar radiation at 65°N diminished, the world entered the MIS6 glacial period, leading to a rapid expansion of the Arctic ice sheet into the middle latitudes (Roe, 2006). This expansion resulted in decreased SST over the Northwest Pacific Ocean and a strengthening of the Siberian-Mongolia high pressure system, which enhanced the sea-land thermal difference in the middle and high latitudes (Xiong et al., 2023). The increasing thermal difference between sea and land in these latitudes intensified the westerly winds (winter winds) (Wu et al., 2011; Kang et al., 2022), resulting in a decreased EASM precipitation (Fig. 9i). Concurrently, the strengthening westerly winds obstructed the southward movement of cold air from high latitudes, leading to elevated surface temperatures in East Asia (Wu et al., 2011). This phenomenon caused the melting of permafrost and marked the onset of the second stage of a “warm and dry” climate in the region. During MIS 5e, the significant rise in Northern Hemisphere summer insolation temporarily enhanced EASM precipitation, which subsequently weakened in alignment with the decline in summer insolation at 65°N (Fig. 9h). Overall, on an orbital scale, the variability of EASM precipitation is primarily governed by high-latitude Northern Hemisphere summer insolation and global ice volume (Ren et al., 2023; Wu et al., 2023).

To further investigate the variation periods of the EASM, we conducted a wavelet power spectrum and spectral analysis on the reconstructed precipitation, Hm, and Gt. The results indicate that since 195 ka, the EASM has exhibited significant periodicities of 17 ka (Fig. 10) and 23 ka (Supplementary Fig. S2). These findings are consistent with the precession period of approximately 20 ka observed in the EASM precipitation, as recorded by the borehole sediments from the Okinawa Trough (Zhao et al., 2023), Sanbao Cave stalagmite  $\delta^{18}\text{O}$  records (Fig. 9c), and climate system models. This suggests that, in addition to high-latitude solar forcing, the evolution of the EASM precipitation in the Songnen Plain since the late Middle Pleistocene is also influenced by low-latitude precession (Cheng et al., 2016; Ren et al., 2025; An et al., 2015; Thomson et al., 2021; Zhao et al., 2023). The precession of low latitudes influences the thermal difference between land and sea primarily by altering the amount of solar radiation received in these regions, which subsequently affects monsoon precipitation. However, this response may not be linear in the mid-latitudes (Li et al., 2024). During periods when changes in summer solar radiation at 30°N are predominantly driven by precession, the reconstructed EASM precipitation exhibits in-phase changes (Figs. 9i, b). An increase in summer solar radiation leads to a heightened sea-land thermal difference, which in turn strengthens monsoon circulation and enhances northward water vapor transport, resulting in increased precipitation in northeast China (Xie and Liu, 2020; Huang et al., 2020). In the middle to late stages of MIS 6, EASM precipitation clearly lags behind variations in solar energy. This delay may be attributed to global cooling, which results in reduced summer solar radiation near 30°N, causing the ocean temperature response to lag behind that of the land (Li et al., 2024). The thermal difference between sea and land at low latitudes is not well-defined (Wang and Zhang, 2020), which hampers the intensification of monsoon circulation and contributes to the lag of EASM precipitation behind changes in solar radiation. Additionally, the reduction in solar radiation may disrupt the southward migration or weakening of the Western Pacific Subtropical High (WPSH, Wang and Zhang, 2020), hindering the transport of water vapor to East Asia and leading to delayed precipitation. Furthermore, studies on the rapid decline of the EASM over the last 2000 years indicate that when solar radiation weakens, atmospheric circulation may transit from an El Niño-like to a La Niña-like state. This shift can cause the position of the WPSH to change, thereby influencing the precipitation intensity of the EASM (Lan et al., 2020). A comparison between the summer insolation at 30°N and the Zonal SST gradient between WPWP and EEP reveals that solar radiation at this latitude transits from weak to its maximum during MIS 5e (Figs. 9a, b), while the EASM continues to weaken until it reaches its lowest (Fig. 9h). This observation suggests that, prior to this period, the SST of the tropical Pacific Ocean may have decreased due to the reduction in solar radiation at low latitudes. This alteration in ocean and atmospheric circulation subsequently triggers the El Niño-Southern Oscillation (ENSO), which, in turn, reduces EASM precipitation (Zhang et al., 2023b).

## 5. Conclusions

The study utilized high-resolution magnetic susceptibility, Gt, Hm, Hm/Gt ratio, and OSL analyses of the Harbin loess-paleosol sequence, alongside analyses of the topsoil in potential dust sources, to investigate the paleoclimatic significance of these proxies in the distinctive black paleosols developed in cold regions, and quantitatively reconstruct variations in paleoprecipitation and paleogleyization in the Songnen Plain. Based on the results obtained, the following conclusions can be drawn:

1. The basal age of the HS loess-paleosol section in Harbin is constrained to 195 ka, indicating the oldest loess accumulation in the Songnen Plain.
2. The  $\chi_{\text{rf}}$  values exhibit minor variations and do not correlate with the changes observed in the stratigraphic lithological characteristics.

The values of the  $\chi_{\text{lf}}$ , Gt and Hm in the black paleosol layers are significantly lower than those found in the loess layers. This suggests that the formation of black paleosol in mid- and high-latitude permafrost regions may be influenced by soil gleyization, which could result in the decoupling of these indexes from the pedogenic processes. In this sense, these indicators can be employed to assess the degree of soil gleyization.

3. The  $\chi_{\text{lf}}$  and Hm/Gt values of the topsoil in the potential dust source areas exhibit an inverse correlation with the MAP. Based on this relationship, the climofunctions for  $\chi_{\text{lf}}\text{-MAP}$  and Hm/Gt-MAP have been proposed to reconstruct the paleoprecipitation and paleogleyization as recorded by the loess-paleosol sequence. The precipitation reconstructed from the  $\chi_{\text{lf}}$  is significantly higher than that derived from the Hm/Gt, and the difference between these two measures can be used to quantitatively characterize the non-monsoon precipitation and the degree of gleyization of the black paleosol. Notably, the loess layers show almost no signs of gleyization, while the gleyization degree of the black paleosol layers ranges from 5.18 % to 11.44 %.

4. The paleoclimatic and paleogleyization evolution of the Songnen Plain since 195 ka can be categorized into three distinct stages: from 195 to 160 ka, the EASM was strong, characterized by a cold and wet climate with a low degree of soil gleyization; from 160 ka to 123 ka, the intensity of the EASM weakened, leading to a warm and dry climate, and an increased degree of soil gleyization; after 123 ka, monsoon precipitation continued to decline, and the climate became cool and dry, while the rate of permafrost melting slowed. However, from 105 to 100 ka, there was a modest increase in temperature and monsoon rainfall, which was accompanied by intensified soil gleyization. In contrast, from 65 to 55 ka, the climate resembled that of the earlier cold interval.

5. Since 195 ka, the evolution of the EASM precipitation has been jointly regulated by both high- and low-latitude processes. On an orbital scale, it is primarily associated with changes in high-latitude summer solar radiation and variations in Arctic ice volume. Additionally, precession-controlled summer solar radiation in the low latitudes also modulates the EASM precipitation. When these factors are in phase, an increase in solar radiation results in heightened EASM precipitation. Conversely, the lagged response of the EASM precipitation may be linked to the southward shift of the WPSH or ENSO events during periods of diminished solar radiation.

## CRediT authorship contribution statement

**Yujia Sun:** Writing – review & editing, Writing – original draft, Software, Methodology, Data curation, Conceptualization. **Yanru Wang:** Writing – review & editing, Writing – original draft, Methodology, Conceptualization. **Yuanyun Xie:** Writing – review & editing, Writing – original draft, Methodology, Conceptualization. **Chunguo Kang:** Visualization, Validation. **Chuanyi Wei:** Writing – review & editing. **Yehui Wang:** Visualization, Validation. **Jie Meng:** Visualization, Validation. **Lei Sun:** Visualization, Validation. **Peng Wu:** Visualization, Validation. **Ruonan Liu:** Visualization, Validation. **Zhenyu Wei:** Visualization, Validation. **Haijin Liu:** Visualization, Validation. **Yunping Chi:** Supervision.

## Declaration of competing interest

The authors declared that they have no conflicts of interest to this work. We declare that we do not have any commercial or associative interest that represents a conflict of interest in connection with the work submitted.

## Acknowledgments

This study was financially supported by the Natural Science Foundation of Heilongjiang Province, China (Grant: ZD2023D003), by National Natural Science Foundation of China (Grant: 42171006 and 41871013), and by Harbin Normal University PhD Start-up Fund (Code:

XKB202312). The authors would like to express our appreciation to luminescence laboratory of Hangzhou Luminescence Detection Technology Co., Ltd. for dating experiment. Thanks to Haodong Qi, Liangchen Zhang, Ying Zhou, Yan Jiao, Yaru Zhao, Qian Ni, and Linli Tao for their participation in the discussion of the paper writing and assistance in sample pretreatment.

## Appendix A. Supplementary data

Supplementary data to this article can be found online at <https://doi.org/10.1016/j.palaeo.2025.113287>.

## Data availability

The authors confirm that all data necessary for supporting the scientific findings of this paper have been provided.

## References

- An, Z.S., Kukla, G., Liu, T.S., 1989. Loess Stratigraphy in Luochuan of China. *Quaternary Sciences* 2, 155–168.
- An, Z.S., Wu, G.X., Li, J.P., Sun, Y.B., Liu, Q.M., Zhou, W.J., Cai, Y.J., Duan, A.M., Li, L., Mao, J.Y., Cheng, H., Shi, Z.G., Tan, L.C., Yan, H., Ao, H., 2015. Global monsoon dynamics and climate change. *Journal of Earth Environment* 6 (6), 341–381. <https://doi.org/10.7515/JEE201506001>.
- Ao, H., Rohling, E.J., Stringer, C., Roberts, A.P., Dekkers, M.J., Dupont-Nivet, G., Yu, J. M., Liu, Q.S., Zhang, P., Liu, Z.H., Ma, X.L., Zhou, W.J., Jin, Z.D., Xiao, G.Q., Wang, H., Sun, Q., Yang, P.G., Peng, X.Z., Shi, Z.G., Qiang, X.K., An, Z.S., 2020. Two-stage mid-Brunhes climate transition and mid-Pleistocene human diversification. *Earth Sci. Rev.* 210, 103354. <https://doi.org/10.1016/j.earscirev.2020.103354>.
- Balsam, L.B., Wagers, A.J., Christensen, J.L., Kofidis, T., Weissman, I.L., Robbins, R.C., 2004. Haematopoietic stem cells adopt mature haematopoietic fates in ischaemic myocardium. *Nature* 428 (6983), 668–673. <https://doi.org/10.1038/nature02460>.
- Balsam, W.L., Ellwood, B.B., Ji, J.F., Williams, E.R., Long, X.Y., Hassani, A.E., 2011. Magnetic susceptibility as a proxy for rainfall: worldwide data from tropical and temperate climate. *Quat. Sci. Rev.* 30, 2732–2744. <https://doi.org/10.1016/j.quascirev.2011.06.002>.
- Beck, J.W., Zhou, W.J., Li, C., Wu, Z.K., White, L., Xian, F., Kong, X.H., An, Z.S., 2018. A 5500-year record of East Asian monsoon rainfall from  $^{10}\text{Be}$  in loess. *Science* 360 (6391), 877–881. <https://doi.org/10.1126/science.aam5825>.
- Bégét, J.E., Stone, D.B., Hawkins, D.B., 1990. Paleoclimate Forcing of Magnetic Susceptibility Variations in Alaskan Loess during the Late Quaternary. *Geology* 18 (1), 40–43. [https://doi.org/10.1130/0091-7613\(1990\)018%3C0040:PFOMSV%3E2.3.CO;2](https://doi.org/10.1130/0091-7613(1990)018%3C0040:PFOMSV%3E2.3.CO;2).
- Berger, A., 1978. Long-term variations of daily insolation and Quaternary climatic changes. *J. Atmos. Sci.*, 35(12), 2362–2367. DOI: doi: [https://doi.org/10.1175/1520-0469\(1978\)035%3C2362:LTVDOD%3E2.0.CO;2](https://doi.org/10.1175/1520-0469(1978)035%3C2362:LTVDOD%3E2.0.CO;2).
- Blaauw, M., Christen, J.A., 2011. Flexible paleoclimate age-depth models using an autoregressive gamma process. *Bayesian Anal.* 3, 457–474. <https://doi.org/10.1214/11-BA618>.
- Blaauw, M., Christen, J.A., Bennett, K.D., Reimer, P.J., 2018. Double the dates and go for Bayes—Impacts of model choice, dating density and quality on chronologies. *Quat. Sci. Rev.* 188, 58–66. <https://doi.org/10.1016/j.quascirev.2018.03.032>.
- Brinkman, R., 1970. Ferrolysis, a hydromorphic soil forming process. *Geoderma* 3 (3), 199–206. [https://doi.org/10.1016/0016-7061\(70\)90019-4](https://doi.org/10.1016/0016-7061(70)90019-4).
- Brinkman, R., 1977. Problem hydromorphic soils in north-East Thailand. 2. Physical and chemical aspects, mineralogy and genesis. *Neth. J. Agric. Sci.* 25 (3), 170–181. <https://doi.org/10.18174/njas.v25i3.17130>.
- Caley, T., Roche, D.M., Renssen, H., 2014. Orbital Asian summer monsoon dynamics revealed using an isotope-enabled global climate model. *Nat. Commun.* 5 (1), 5371. <https://doi.org/10.1038/ncomms6371>.
- Cao, Z., Zhu, X.D., 2014. Research on the formation reason of loess in middle and eastern place in Northeast China. *Journal of Chang chun Normal University: Natural Science* 2, 85–89.
- Cao, J., Wang, B., Liu, J., 2019. Attribution of the last Glacial Maximum climate formation. *Clim. Dyn.* 53, 1661–1679. <https://doi.org/10.1007/s00382-019-04711-6>.
- Chen, H., Yang, S.L., Cheng, T., Liu, N.N., Li, S., Liang, M.H., Tang, G.G., 2018. The magnetic susceptibility of top soil in the eastern Tibetan Plateau: features and environmental implications [J]. *J. Glaciol. Geocryol.* 40 (6), 1187–1194.
- Cheng, H., Edwards, R.L., Sinha, A., Spötl, C., Yi, L., Chen, S.T., Kelly, M., Kathayat, G., Wang, X.F., Li, X.L., Kong, X.G., Wang, Y.J., Ning, Y.F., Zhang, H.W., 2016. The Asian monsoon over the past 640,000 years and ice age terminations. *nature* 534 (7609), 640–646. <https://doi.org/10.1038/nature18591>.
- Chlachula, J., 2003. The Siberian loess record and its significance for reconstruction of Pleistocene climate change in north-Central Asia. *Quat. Sci. Rev.* 22 (18–19), 1879–1906. [https://doi.org/10.1016/S0277-3791\(03\)00182-3](https://doi.org/10.1016/S0277-3791(03)00182-3).
- Chu, B.J., Gao, Z.C., Yang, S.S., Xi, X.H., 1988. Quaternary magnetostratigraphic classification of the Songnen Plain (Songhuajiang River-Nenjiang River Plain). *Mar. Geol. Quat. Geol.* 8 (4), 91–96. <https://doi.org/10.16562/j.cnki.0256-1492.1988.04.014>.
- Cui, H.S., Zhang, B., Yu, L., Zhu, J.H., He, Y.F., 2003. Pattern and change of black soil resources in China. *Resour Sci* (03),64–68. DOI: <https://doi.org/10.3321/j.issn:1007-7588.2003.03.010>.
- Cornell, R.M., Schwertmann, U., 2003. *The iron Oxides: Structure, Properties, Reactions, Occurrences, and Uses*, vol. 664. Wiley-vch, Weinheim.
- Deaton, B.C., Balsam, W.L., 1991. Visible spectroscopy- a rapid method for determining hematite and goethite concentration in geological materials: Research method paper. *J. Sediment. Res.* 61 (4), 628–632.
- Deng, C.L., Shaw, J., Liu, Q.S., Pan, Y.X., Zhu, R.X., 2006. Mineral magnetic variation of the Jingbian loess/paleosol sequence in the northern Loess Plateau of China: Implications for Quaternary development of Asian aridification and cooling. *Earth Planet. Sci. Lett.* 241 (1–2), 248–259. <https://doi.org/10.1016/j.epsl.2005.10.020>.
- Ding, Z.L., Ranov, V., Yang, S.L., Finaev, A., Han, J.M., Wang, G.A., 2002. The loess record in southern Tajikistan and correlation with Chinese loess. *Earth Planet. Sci. Lett.* 200 (3–4), 387–400. [https://doi.org/10.1016/S0012-821X\(02\)00637-4](https://doi.org/10.1016/S0012-821X(02)00637-4).
- Du, H.R., Xie, Y.Y., Kang, C.G., Chi, Y.P., Wang, J.X., Sun, L., 2020. Grain-size and geochemical compositions of the Harbin loess deposits and their implications for eolian dust provenances. *J. Desert Res.* 40 (1), 64–76. <https://doi.org/10.7522/j.issn.1000-694X.2019.00046>.
- Fan, L.F., Kuang, X.X., Guo, Z.L., Zhang, R., Zheng, C.M., 2024. Impacts of permafrost degradation on streamflow in the northern Himalayas. *Sci. Sin. Terra* 54 (6), 2020–2030. <https://doi.org/10.1360/N072023-0300>.
- Fey, M.V., 1983. Hypothesis for the pedogenic yellowing of red soil materials. *Techn. Commun., Dept. Agric. Fisheries Rep. South Africa* 18, 130–136.
- Gao, Y.X., Xu, S.Y., Guo, Q.Y., Zhang, M.L., 1962. Monsoon regions in China and regional climates. In: Gao, Y.X. (Ed.), *Some Problems on East-Asia Monsoon*. Science Press, Beijing, pp. 49–63.
- Gao, Z.Q., Song, Y.F., Guan, X.M., 1988. Study on some physical and chemical properties of the formation process of white clay. *Acta Pedol. Sin.* 01, 13–21.
- Gao, X.B., Hao, Q.Z., Wang, L., Oldfield, F., Bloemendal, J., Deng, C.L., Song, Y., Ge, J.Y., Wu, H.B., Xu, B., Li, F.J., Han, L., Fu, Y., Guo, Z.T., 2018. The different climatic response of pedogenic hematite and ferrimagnetic minerals: evidence from particle-sized modern soils over the Chinese Loess Plateau. *Quat. Sci. Rev.* 179, 69–86. <https://doi.org/10.1016/j.quascirev.2017.11.011>.
- George, K., Friedrich, H., Liu, X.M., Xu, T.C., Liu, T.S., An, Z.S., 1988. Pleistocene climates in China dated by magnetic susceptibility. *Geology* 16 (9), 811–814. [https://doi.org/10.1130/0091-7613\(1988\)016%3C811:PCICDB%3E2.3.CO;2](https://doi.org/10.1130/0091-7613(1988)016%3C811:PCICDB%3E2.3.CO;2).
- Gianella, S., Girardi, F., Ischia, G., Lonardelli, I., Mattarelli, M., Montagna, M., 2010. On the goethite to hematite phase transformation. *J. Therm. Anal. Calorim.* 102, 867–873. <https://doi.org/10.1007/s10973-010-0756-2>.
- Giosan, L., Flood, R.D., Grützner, J., Mudie, P., 2002. Paleoceanographic significance of sediment color on western North Atlantic drifts: II. Late Pliocene–Pleistocene sedimentation. *Mar. Geol.* 189 (1–2), 43–61. [https://doi.org/10.1016/S0025-3227\(02\)00322-5](https://doi.org/10.1016/S0025-3227(02)00322-5).
- Gualtieri, A.F., Venturelli, P., 1999. In situ study of the goethite-hematite phase transformation by real time synchrotron powder diffraction. *Am. Mineral.* 84, 895–904. <https://doi.org/10.2138/am-1999-5-624>.
- Guo, Z.T., Biscaye, P., Wei, L.Y., Chen, X.H., Peng, S.Z., Liu, T.S., 2000. Summer monsoon variations over the last 1.2 Ma from the weathering of loess-soil sequences in China. *Geophys. Res. Lett.* 27 (12), 1751–1754. <https://doi.org/10.1029/1999GL008419>.
- Guo, X.L., Liu, X.M., Guo, H., Chen, Q., Li, P.Y., Ma, M.M., Liu, Z., 2012. The magnetic Mechanism of SS paleosol in BaoJi section. *Quaternary Science* 32 (4), 785–794. <https://doi.org/10.3969/j.issn.1001-7410.2012.04.24>.
- Guo, F.Z., Chi, Y.P., Xie, Y.Y., Kang, C.G., Liu, R.N., Sun, L., Wu, P., Wei, Z.Y., Liu, H.J., 2024. The Meridional Variation Characteristics of Iron-Bearing Minerals in Surface Sediments of Otinad Sandy Land and its Environmental Significance Acta Sedimentologica Sinica, pp. 1–18. DOI: 10.14027 / j.i SSN 1000-0550.2024.070.
- Hao, Q.Z., Oldfield, F., Bloemendal, J., Torrent, J., Guo, Z.T., 2009. The record of changing hematite and goethite accumulation over the past 22 Myr on the Chinese Loess Plateau from magnetic measurements and diffuse reflectance spectroscopy. *J. Geophys. Res. Solid Earth* 114 (B12). <https://doi.org/10.1029/2009JB006604>.
- He, Z., Hou, R.J., Fu, Q., Li, T.X., Zhang, S.J., Su, A.S., 2023. Evolution mechanism of soil hydrothermal parameters under freeze-thaw cycles: Regulatory significance of straw and biochar. *J. Clean. Prod.* 385, 135787. <https://doi.org/10.1016/j.jclepro.2022.135787>.
- Heil, J.C.W., King, J.W., Zárate, M.A., Schultz, P.H., 2010. Climatic interpretation of a 1.9 Ma environmental magnetic record of loess deposition and soil formation in the central eastern Pampas of Buenos Aires, Argentina. *Quat. Sci. Rev.* 29 (19–20), 2705–2718. <https://doi.org/10.1016/j.quascirev.2010.06.024>.
- Heller, F., Liu, T.S., 1984. Magnetism of Chinese loess deposits. *Geophys. J. Int.* 77 (1), 125–141. <https://doi.org/10.1111/j.1365-246X.1984.tb01928.x>.
- Heller, F., Liu, T.S., 1986. Palaeoclimatic and sedimentary history from magnetic susceptibility of loess in China. *Geophys. Res. Lett.* 13 (11), 1169–1172. <https://doi.org/10.1029/GL013i011p01169>.
- Heller, F., Liu, X.M., Liu, T.S., Xu, T.C., 1991. Magnetic susceptibility of loess in China. *Earth Planet. Sci. Lett.* 103 (1–4), 301–310. [https://doi.org/10.1016/0012-821X\(91\)90168-H](https://doi.org/10.1016/0012-821X(91)90168-H).
- Hou, S.M., 2016. Mechanism of Magnetization Rate Change in the Kurtak Profile in Siberia and its Paleoclimatic Significance[D]. Fujian Normal University.
- Hu, P.X., Liu, Q.S., 2014. The production and transformation of magnetic minerals during pedogenesis and its paleoclimatic significance. *Quaternary Sciences* 03, 458–473. <https://doi.org/10.3969/j.issn.1001-7410.2014.03.02>.

- Huang, L.M., Jia, X.X., Shao, M.A., Chen, L.M., Han, G.Z., Zhang, G.L., 2018. Phases and rates of iron and magnetism changes during paddy soil development on calcareous marine sediment and acid Quaternary Red-Clay. *Sci. Rep.* 8, 444. <https://doi.org/10.1038/s41598-017-18963-x>.
- Huang, E.Q., Wang, P.X., Wang, Y., Yan, M., Tian, J., Li, S.H., Ma, W.T., 2020. Dole effect as a measurement of the low-latitude hydrological cycle over the past 800 ka. *Sci. Adv.* 6 (41), eaba4823. <https://doi.org/10.1126/sciadv.eaba4823>.
- Hyland, E.G., Sheldon, N.D., Van der Voo, R., Badgley, C., Abrajevitch, A., 2015. A new paleoprecipitation proxy based on soil magnetic properties: implications for expanding paleoclimate reconstructions. *Geol. Soc. Am. Bull.* <https://doi.org/10.1130/B31207.1>.
- Ji, J.F., Balsam, W., Chen, J., 2001. Mineralogic and climatic interpretations of the Luochuan loess section (China) based on diffuse reflectance spectrophotometry. *Quat. Res.* 56 (1), 23–30. <https://doi.org/10.1006/qres.2001.2238>.
- Ji, J.F., Balsam, W., Chen, J., Liu, L.W., 2002. Rapid and quantitative measurement of hematite and goethite in the Chinese loess-paleosol sequence by diffuse reflectance spectroscopy. *Clays and Clay minerals*, 50(2), 208–216. <https://doi.org/10.1346/000986002760832801>.
- Ji, J.F., Chen, J., Balsam, W., Lu, H.Y., Sun, Y.B., Xu, H.F., 2004. High resolution hematite/goethite records from Chinese loess sequences for the last glacial-interglacial cycle: Rapid climatic response of the East Asian Monsoon to the tropical Pacific. *Geophys. Res. Lett.* 31 (3). <https://doi.org/10.1029/2003GL018975>.
- Ji, J.F., Chen, J., Balsam, W., Liu, L.W., Chen, Y., Zhao, L., Zhou, W., 2007. Quantitative analysis of hematite and goethite in the chinese loess-paleosol sequences and its implication for dry and humid variability. *Quaternary Sciences* 27 (2), 221–229. <https://doi.org/10.3321/j.issn.1001-7410.2007.02.007>.
- Jia, J., Lu, H., Wang, Y.J., Xia, D.S., 2018. Variations in the iron mineralogy of a loess section in Tajikistan during the Mid-Pleistocene and late Pleistocene: Implications for the climatic evolution in Central Asia. *Geochem. Geophys. Geosyst.* 19 (4), 1244–1258. <https://doi.org/10.1002/2017GC007371>.
- Jiang, Z.X., Liu, Q.S., 2016. Quantification of hematite and its climatic significances. *Quaternary Sciences* 36 (3), 676–689. <https://doi.org/10.11928/j.issn.1001-7410.2016.03.17>.
- Jiao, W.J., Wan, S.M., Li, Y.X., Zhao, D.B., Liu, C., Jin, H.L., Li, M.J., Yu, Z.J., Zhang, J., Pei, W.Q., Li, A.C., 2023. Global Cooling-Driven Summer Monsoon weakening in South China across the Eocene-Oligocene transition. *J. Geophys. Res. Solid Earth* 128 (11), e2023JB027265. <https://doi.org/10.1029/2023JB027265>.
- Jordanova, D., Jordanova, N., 2021. Updating the significance and paleoclimate implications of magnetic susceptibility of Holocene loessic soils. *Geoderma* 391, 114982. <https://doi.org/10.1016/j.geoderma.2021.114982>.
- Kalm, V.E., Rutter, N.W., Rokosh, C.D., 1996. Clay minerals and their paleoenvironmental interpretation in the Baoji loess section, Southern Loess Plateau, China. *Catena* 27 (1), 49–61. [https://doi.org/10.1016/0341-8162\(96\)00008-2](https://doi.org/10.1016/0341-8162(96)00008-2).
- Kang, S.G., Wang, X.L., Du, J.H., Song, Y.G., 2022. Paleoclimates inform on a weakening and amplitude-reduced East Asian winter monsoon in the warming future. *Geology* 50 (11), 1224–1228. <https://doi.org/10.1130/G50246.1>.
- Kong, X.H., Zhou, W.J., Beck, J.W., Xian, F., Qiang, X.K., Ao, H., Wu, Z.K., An, Z.S., 2020. Loess magnetic susceptibility flux: a new proxy of East Asian monsoon precipitation. *J. Asian Earth Sci.* 201, 104489. <https://doi.org/10.1016/j.jseas.2020.104489>.
- Lan, J.H., Xu, H., Lang, Y.G., Yu, K.K., Zhou, P., Kang, S.G., Zhou, K.E., Wang, X.L., Wang, T.L., Cheng, P., Yan, D.N., Yu, S.Y., Che, P., Ye, Y.D., Tan, L.C., 2020. Dramatic weakening of the East Asian summer monsoon in northern China during the transition from the medieval warm period to the Little Ice Age. *Geology* 48 (4), 307–312. <https://doi.org/10.1130/G46811.1>.
- Laskar, J., Robutel, P., Joutel, F., Gaspineau, M., Correia, A.C., Levrard, B., 2004. A long-term numerical solution for the insolation quantities of the Earth. *Astron. Astrophys.* 428 (1), 261–285. <https://doi.org/10.1051/0004-6361:20041335>.
- Lepre, C.J., Olsen, P.E., 2021. Hematite reconstruction of late Triassic hydroclimate over the Colorado Plateau. *Proc. Natl. Acad. Sci.* 118 (7), e2004343118. <https://doi.org/10.1073/pnas.2004343118>.
- Li, X., Cai, Y.F., 2014. The colouration mechanism and genetic study of cretaceous oceanic red beds. *Acta Mineral. Sin.* 34 (4), 451–460. <https://doi.org/10.16461/j.cnki.1000-4734.2014.04.006>.
- Li, J.W., Liu, B., 2024. Variation in Hematite Content in Loess-Paleosol at Different Latitudes and its Climatic significance: based on Diffuse Reflectance Spectroscopy and Chromaticity Methods. *Journal of Fujian Normal University (Natural Science Edition)* 40.04 (2024), 1–10. DOI: 10.12046 / j. issn. 1000-5277. 2024. 04. 001.
- Li, C., Yang, S.Y., 2012. Hematite and Goethite distribution in the Yangtze River Sediments by using Diffused Reflectance Spectroscopy. *Earth Sciences (Journal of China University of Geosciences)* 37 (z1), 11–19. <https://doi.org/10.3799/dqkx.2012.S1.002>.
- Li, M.S., Hinnov, L., Kump, L., 2019a. Acycle: Time-series analysis software for paleoclimate research and education. *Comput. Geosci.* 127, 12–22. <https://doi.org/10.1016/j.cageo.2019.02.011>.
- Li, X.C., Yang, Z.Z., Zhang, C., Wei, J.J., Zhang, H.Q., Li, Z.H., Chi, M., Wang, M.S., Chen, J.Q., Hu, J.W., 2019b. Effects of different crystalline iron oxides on immobilization and bioavailability of Cd in contaminated sediment. *Chem. Eng.* 373, 307–317. <https://doi.org/10.1016/j.cej.2019.05.015>.
- Li, Y.L., Fu, Q., Li, T.X., Liu, D., Hou, R.J., Li, Q.L., Li, J., Li, M., Meng, F.X., 2021. Snow melting water infiltration mechanism of farmland freezing-thawing soil and determination of meltwater infiltration parameter in seasonal frozen soil areas. *Agric. Water Manag.* 258, 107165. <https://doi.org/10.1016/j.agwat.2021.107165>.
- Li, M.Y., Zhang, X.T., Liu, H.Y., Wei, S.Q., 2022. Effects of Water Management on the Transformation of Iron Oxide Forms in PaddySoils and Its Coupling with Changes in Cadmium Activity. *Environ. Sci.* 43 (08), 4301–4312. <https://doi.org/10.13227/j.hjkx.202111108>.
- Li, X.S., Zhou, Y.W., Han, Z.Y., Yuan, X.K., Yi, S.W., Zeng, Y.Q., Qin, L.S., Lu, M., Lu, H.Y., 2024. Loess deposits in the low latitudes of East Asia reveal the ~ 20-kyr precipitation cycle. *Nat. Commun.* 15 (1), 1023. <https://doi.org/10.1038/s41467-024-45379-9>.
- Lisiecki, L.E., Raymo, M.E., 2005. A Pliocene-Pleistocene stack of 57 globally distributed benthic  $\delta^{18}\text{O}$  records. *Paleoceanography* 20 (1). <https://doi.org/10.1029/2004PA001071>.
- Liu, T.S., 1985. *Loess and the Environment*. China Ocean Press.
- Liu, Z.F., Liu, Q.S., 2013. Magnetic properties of soil profiles with different slopes in Yan'an, Shaanxi Province and their significance in the reconstruction of ancient rainfall. *Sci. China Earth Sci.* 12, 2037–2048.
- Liu, X.M., Shaw, J., Liu, T.S., Heller, F., Yuan, B.Y., 1992. Magnetic mineralogy of Chinese loess and its significance. *Geophys. J. Int.* 108 (1), 301–308. <https://doi.org/10.1111/j.1365-246X.1992.tb00859.x>.
- Liu, Q.S., Deng, C.L., Torrent, J., Zhu, R.X., 2007. Review of recent developments in mineral magnetism of the Chinese loess. *Quat. Sci. Rev.* 26 (3–4), 368–385. <https://doi.org/10.1016/j.quascirev.2006.08.004>.
- Liu, X.M., Liu, T.S., Xia, D.S., Hesse, P., Chlachula, J., Wang, G., 2007a. Paleoclimate record of magnetization of loess in China and Siberia—analysis of two soil formation models under oxidation and reduction conditions. *Science in China Press* 37 (10), 1382–1391. <https://doi.org/10.3969/j.issn.1674-7240.2007.10.010>.
- Liu, X.M., Xia, D.S., Liu, Z.L., Ding, Z.L., Chen, F.H., Begét, J.E., 2007b. Discussion on two models of paleoclimate records of magnetic susceptibility of Alaskan and Chinese loess. *Quaternary Science* 27 (2), 210–220. <https://doi.org/10.3321/j.issn:1001-7410.2007.02.006>.
- Liu, X.M., Liu, T.S., Xia, D.S., Hesse, P., Chlachula, J., Wang, G., 2008. Two pedogenic models for paleoclimate records of magnetic susceptibility from Chinese and Siberian loess. *Sci. China Earth Sci.* 51, 284–293. <https://doi.org/10.1007/s11430-007-0145-2>.
- Liu, X., Liu, T.S., Xia, D.S., 2008b. The analysis of two different pedogenesis models in reductive and oxidative conditions record by Chinese Siberia loess. *Sci. China Earth Sci.* 37, 1382–1391.
- Liu, Q.S., Torrent, J., Barron, V., Duan, Z.Q., Bloemendal, J., 2011. Quantification of hematite from the visible diffuse reflectance spectrum: effects of aluminium substitution and grain morphology. *Clay Miner.* 46, 137–147. <https://doi.org/10.1180/claymin.2011.046.1.137>.
- Liu, Y., Shi, Z.T., Deng, C.L., Su, H., Zhang, W.X., 2012. Mineral magnetic investigation of the Taledo loess-paleosol sequence since the last interglacial in the Yili Basin in the Asian interior. *Geophys. J. Int.* 190 (1), 267–277. <https://doi.org/10.1111/j.1365-246X.2012.05527.x>.
- Liu, Q.S., Jin, C.S., Hu, P.X., Jiang, Z.X., Ge, K.P., Roberts, A.P., 2015. Magnetostriatigraphy of Chinese loess-paleosol sequences. *Earth Sci. Rev.* 150, 139–167. <https://doi.org/10.1016/j.earscirev.2015.07.009>.
- Liu, X.K., Liu, R.J., Li, Z.Q., Du, J., Jia, F.F., Li, T.F., Chen, L., Wu, Y.Q., 2017. Magnetic susceptibility of surface soils in the Mu Us Desert and its environmental significance. *Aeolian Res.* 25, 127–134. <https://doi.org/10.1016/j.aeolia.2017.04.003>.
- Liu, Y.M., Liu, X.X., Ma, L., Kang, S.G., Qiang, X.K., Guo, F., Sun, Y.B., 2020. Temporal-spatial variations in aeolian flux on the Chinese Loess Plateau during the last 150 ka. *Geol. Mag.* 157 (5), 757–767. <https://doi.org/10.1017/S0016756819001067>.
- Liu, J.H., Chi, Y.P., Xie, Y.Y., Kang, C.G., Wei, Z.Y., Wu, P., Sun, L., 2023. Geochemical characteristics of Songnen Sandy Land and indication of its contribution to aeolian dust. *J. Desert Res.* 03, 252–263. <https://doi.org/10.7522/j.issn.1000-694X.2022.00149>.
- Long, X.Y., Ji, J.F., Balsam, W., 2011. Rainfall-dependent transformations of iron oxides in a tropical saprolite transect of Hainan Island, South China: Spectral and magnetic measurements. *J. Geophys. Res.* 116 (F3). <https://doi.org/10.1029/2010JF001712>.
- Long, X.Y., Ji, J.F., Barron, V., Torrent, J., 2016. Climatic thresholds for pedogenic iron oxides under aerobic conditions: Processes and their significance in paleoclimate reconstruction. *Quat. Sci. Rev.* 150, 264–277. <https://doi.org/10.1016/j.quascirev.2016.08.031>.
- Lu, S.G., 1999. A Comparative Study on magnetic Minerals of Red Soil and Paddy Soil. *Bull. Sci. Technol.* 15, 409–413. <https://doi.org/10.13774/j.cnki.kjtb.1999.06.001>.
- Lu, H.Y., 2015. Driving force behind global cooling in the Cenozoic: an ongoing mystery. *Sci. Bull.* 60 (24), 2091–2095. <https://doi.org/10.1007/s11434-015-0973-y>.
- Lu, H.Y., An, Z.S., 1997. Paleoclimate significance of grain size composition of Luochuan loess. *Chin. Sci. Bull.* 01, 66–69.
- Lu, H.Y., An, Z.S., 1998. Paleoclimate significance of grain size of loess-paleosol deposit in Chinese Loess Plateau. *Sci. China Ser. D Earth Sci.* 41, 626–631.
- Lü, Z.S., Xu, Q., 1991. Some problems in the study of soil white pulping process. *Adv. Soil Sci.* 6:11–16, 43.
- Lü, Z.S., Xu, Q., 1993. *Study on Chinese white clay – I. Characteristics of mechanical composition and geochemical differentiation of elements of white clay*. *Acta Pedol. Sin.* 03, 274–288.
- Lü, B., Liu, X.M., Guo, H., Zhang, X.F., Chen, Z.X., He, M.J., Zhao, G.Y., 2019. Magnetic Properties of the cretaceous Shaxian Formation Stratum in Fujian Province and their Environmental significance. *Acta Sedimentol. Sin.* (03) : 519–531. Doi: 10.14027 / j. issn. 1000-5500.2018.155.
- Ma, M.M., Liu, X.M., Pillans, B.J., Hu, S.Y., Lü, B., Liu, H.F., 2013. Magnetic properties of dashing rocks loess at Timaru, South Island, New Zealand. *Geophys. J. Int.* 195 (1), 75–85. <https://doi.org/10.1093/gji/ggt206>.
- Maher, B.A., Thompson, R., 1995. Paleorainfall reconstructions from pedogenic magnetic susceptibility variations in the Chinese loess and paleosols. *Quat. Res.* 44 (3), 383–391. <https://doi.org/10.1006/qres.1995.1083>.

- Matsuzaki, K.M., Nishi, H., Suzuki, N., Cortese, G., Eynaud, F., Takashima, R., Takashima, R., Kawate, Y., Sakai, T., 2014. Paleoceanographic history of the Northwest Pacific Ocean over the past 740 kyr, discerned from radiolarian fauna. *Palaeogeogr. Palaeoclimatol. Palaeoecol.* 396, 26–40. <https://doi.org/10.1016/j.palaeo.2013.12.036>.
- Meng, X.Q., Liu, L.W., Wang, X.T., Balsam, W., Chen, J., Ji, J.F., 2018. Mineralogical evidence of reduced East Asian summer monsoon rainfall on the Chinese loess plateau during the early Pleistocene interglacials. *Earth Planet. Sci. Lett.* 486, 61–69. <https://doi.org/10.1016/j.epsl.2017.12.048>.
- Muñoz Sabater, J., 2019. ERA5-Land monthly averaged data from 1950 to present. Copernicus climate Change Service (C3S) climate data Store (CDS). DOI: 10.24381/cds.68d2bb03 (Accessed on DD-MMM-YYYY).
- Murray, A.S., Wintle, A.G., 2000. Luminescence dating of quartz using an improved single aliquot regenerative-dose protocol. *Radiat. Meas.* 32(1):5773. [https://doi.org/10.1016/S1350-4487\(99\)00253-X](https://doi.org/10.1016/S1350-4487(99)00253-X).
- Najafi, H., Karimi, A., Haghnia, G.H., Khormali, F., Ayoubi, S., Tazikeh, H., 2019. Paleopedology and magnetic properties of sari loess-paleosol sequence in Caspian lowland, northern Iran. *J. Mt. Sci.* 16, 1559–1570. <https://doi.org/10.1007/s11629-019-5446-3>.
- Paterson, G.A., Heslop, D., 2015. New methods for unmixing sediment grain size data. *Geochem. Geophys. Geosyst.* 16 (12), 4494–4506. <https://doi.org/10.1002/2015GC006070>.
- Pavlinov, B.H., Yu, P.X., Shi, S.M., Liu, M.H., Liu, X., Chang, C.F., 1956. Genesis of loess in China. *Chin. Sci. Bull.*, 1(11):1 ~ 15.
- Peng, J., Lian, X., Li, H.P., Huang, C.Q., 2021. Characteristics and environmental significance of cutan in S5-1 paleosol on southern Chinese Loess Plateau. *Journal of huazhong agricultural university* 01, 195–201. <https://doi.org/10.13300/j.cnki.hnlkxb.2021.01.024>.
- Pepe, D.J., Evans, D.A.D., Smirnov, A.V., 2009. Magnetostratigraphy of the Ludlow Member of the Fort Union Formation (lower Paleocene) of the Williston Basin in North Dakota. *Geol. Soc. Am. Bull.* 121, 65–79. <https://doi.org/10.1130/B26353.1>.
- Pineau, A., Kanari, N., Gaballa, I., 2007. Kinetics of reduction of iron oxides by H<sub>2</sub>: Part II. Low temperature reduction of magnetite. *Thermochim. Acta* 456 (2), 75–88. <https://doi.org/10.1016/j.tca.2005.10.004>.
- Qiu, S.W., 2008. *Geomorphology and Quaternary Geology and Application in Northeastern China*. Jilin Science and Technology Press, Changchun, pp. 114–124.
- Ren, B.Z., Hou, H.X., Sui, Y., Wang, Z.X., Cao, M.M., Zhan, Z.D., Shi, L.F., Xi, G.Y., Shao, X.K., Li, L.Y., Li, J.H., 2023. Climate change at orbital scale in Songnen Plain during the Middle and late Pleistocene. *Geol. Bull. China* 1–18. <https://link.cnki.net/urlid/11.4648.P.20231225.1745.003>.
- Ren, Z.X., Chen, W., Wang, L., Chen, S.F., Piao, J.L., 2025. Comparative analysis of east Asian summer monsoon northern boundary indices: variability, climate anomalies and driving mechanisms. *Clim. Dyn.* 63 (1), 1–22. <https://doi.org/10.1007/s00382-024-07526-2>.
- Roe, G., 2006. In defense of Milankovitch. *Geophys. Res. Lett.* 33 (24). <https://doi.org/10.1029/2006GL027817>.
- Schwertmann, U., 1971. Transformation of hematite to goethite in soils. *Nature* 232, 274–285.
- Schwertmann, U., Murad, E., Schulze, D.G., 1982. Is there Holocene reddening (hematite formation) in soils of arid temperate areas? *Geoderma* 27 (3), 209–223. [https://doi.org/10.1016/0016-7061\(82\)90031-3](https://doi.org/10.1016/0016-7061(82)90031-3).
- Shao, X.K., Hou, H.X., Ren, B.Z., Shi, L.F., Zhan, Z.D., Xi, G.Y., Li, J.H., Cao, L.Y., Gao, Y., 2024. Sedimentary characteristics analysis and paleoenvironmental restoration of the ground substrate in Baiquan County, Qiqihar area, Songnen Plain. *Geological Bulletin of China* 43 (9), 1498–1514. <https://doi.org/10.12097/gbc.2023.08.039>.
- Song, H.N., Wang, E.B., Liu, M.X., Duan Mi, X., Ma, Z.Y., Chen, Z., Xin, Y.T., Zhang, H.C., Liu, T., 2024. Grain-size characteristics and genesis of Bayan loess in the eastern of Songnen Plain. *Chinese Journal of Geology* 59 (6), 1748–1758. <https://doi.org/10.12017/dzgx.2024.119>.
- Strani, F., DeMiguel, D., Alba, D.M., Moyà-Solà, S., Bellucci, L., Sardella, R., Madurell-Malapeira, J., 2019. The effects of the ‘0.9 Ma event’ on the Mediterranean ecosystems during the Early–Middle Pleistocene transition as revealed by dental wear patterns of fossil ungulates. *Quat. Sci. Rev.* 210, 80–89. <https://doi.org/10.1016/j.quascirev.2019.02.027>.
- Sun, J.Z., Wang, Y.Y., Zhang, Q.Y., 1982. Division of Quaternary strata in Songliao Plain—application of several chronological methods. *Journal of Chang'an College of Geology* 79–91.
- Sun, L., Shen, B., Sui, B., Huang, B.H., 2017. The influences of East Asian Monsoon on summer precipitation in Northeast China. *Clim. Dyn.* 48, 1647–1659. <https://doi.org/10.1007/s00382-016-3165-9>.
- Sun, Y.B., Yin, Q.Z., Crucifix, M., Clemens, S.C., Araya-Melo, P., Liu, W.G., Qiang, X.K., Liu, Q.S., Zhao, H., Liang, L.J., Chen, H.Y., Li, Y., Zhang, L., Dong, G.C., Li, M., Zhou, W.J., Berger, A., An, Z.S., 2019. Diverse manifestations of the mid-Pleistocene climate transition. *Nat. Commun.* 10, 352. <https://doi.org/10.1038/s41467-018-08257-9>.
- Sun, Y.B., Wang, T., Yin, Q.Z., Lyu, A., Crucifix, M., Cai, Y.J., Ai, L., Clemens, S., An, Z.S., 2022. A review of orbital-scale monsoon variability and dynamics in East Asia during the Quaternary. *Quat. Sci. Rev.* 288, 107593. <https://doi.org/10.1016/j.quascirev.2022.107593>.
- Sun, L., Xie, Y.Y., Kang, C.G., Chi, Y.P., Wu, P., Wei, Z.Y., Li, S.Q., Zhao, Q., Liu, S., 2023. Provenance evidence for the early-to-middle Pleistocene drainage reorganization of the Songhua River. NE China. *Catena* 224, 107004. <https://doi.org/10.1016/j.catena.2023.107004>.
- Thiel, C., Buylaert, J.P., Murray, A., Terhorst, B., Hofer, I., Tsukamoto, S., Frechen, M., 2011. Luminescence dating of the Stratzing loess profile (Austria)—Testing the potential of an elevated temperature post-IR IRSL protocol. *Quat. Int.* 234 (1–2), 23–31. <https://doi.org/10.1016/j.quaint.2010.05.018>.
- Thomson, J.R., Holden, P.B., Anand, P., Edwards, N.R., Porcher, C.A., Harris, N.B.W., 2021. Tectonic and climatic drivers of Asian monsoon evolution. *Nat. Commun.* 12, 4022. <https://doi.org/10.1038/s41467-021-24244-z>.
- Torrent, J., Guzman, R., Parra, M.A., 1982. Influence of relative humidity on the crystallization of Fe (III) oxides from ferrihydrite. *Clay Clay Miner.* 30 (5), 337–340. <https://doi.org/10.1346/CCMN.1982.0300503>.
- Torrent, J., Liu, Q.S., Bloemendal, J., Barrón, V., 2007. Magnetic enhancement and iron oxides in the upper Luochuan loess–paleosol sequence, Chinese Loess Plateau. *Soil Sci. Soc. Am. J.* 71 (5), 1570–1578. <https://doi.org/10.2136/sssaj2006.0328>.
- Torrent, J., Liu, Q., Barrón, V., 2010. Magnetic susceptibility changes in relation to pedogenesis in a Xeralf chronosequence in northwestern Spain. *Eur. J. Soil Sci.* 61, 161–173. <https://doi.org/10.1111/j.1365-2389.2009.01216.x>.
- Trolard, F., Tardy, Y., 1987. The stabilities of gibbsite, boehmite, aluminous goethites and aluminous hematites in bauxites, ferricretes and laterites as a function of water activity, temperature and particle size. *Geochim. Cosmochim. Acta* 51 (4), 945–957. [https://doi.org/10.1016/0016-7037\(87\)90107-4](https://doi.org/10.1016/0016-7037(87)90107-4).
- Wang, J.L., 1993. Study on terrace of Harbin section of Songhua River. *Science of Geography* 1, 87–90.
- Wang, Y.X., 2022. Research on Water Migration in Unsaturated Frozen Soil under Snow Melting Conditions (Master’s Thesis, Southwest Jiaotong University). master.
- Wang, J.Y., Gong, K.Y., 2024. Impacts of permafrost melting on climate change and human society. *Low carbon world* (01) 14(1):40–42. <https://doi.org/10.3969/j.issn.2095-2066.2024.01.014>.
- Wang, J.M., Yan, B.H., Wu, S., Yang, J.W., Zhang, S., Song, C.H., 2012. Climate changes recorded by colors of the Miocene sediments in northeast Qaidam Basin. *Gansu Geology* 21 (1), 6–11.
- Wang, Q.S., Song, Y.G., Zhao, Z.J., Li, J.J., 2016. Color characteristics of Chinese loess and its paleoclimatic significance during the last glacial–interglacial cycle. *J. Asian Earth Sci.* 116, 132–138. <https://doi.org/10.1016/j.jseas.2015.11.013>.
- Wang, Z.D., Huang, C.C., Yang, H.J., Pang, J.L., Cha, X.C., Zhou, Y.L., 2018. Loess Provenance Characteristics and Evolution Indicated by grain size since late Pleistocene at the Eastern Foot of Liupan Mountains, China. *Geography science* 38 (5), 818–826. <https://doi.org/10.13249/j.carol.carroll.nki.SGS.2018.05.020>.
- Wang, J.X., Xie, Y.Y., Kang, C.G., Chi, Y.P., Wu, P., Wei, Z.Y., Sun, L., 2020a. The indication of the heavy mineral characteristics of the core in Harbin Huangshan to the Quaternary drainage evolution of Songhua River. *Quaternary Sciences* 40 (1), 79–94. <https://doi.org/10.11928/j.issn.1001-7410.2020.01.08>.
- Wang, Y., Dong, J., Yang, J.S., 2020b. Quaternary Stratigraphy of the Huangshan Section in Harbin. *Earth Sci.* 07, 2662–2672.
- Wang, Z.Q., Zhang, X., 2020. Changes in the north boundary of the east asian summer monsoon in interglacials of last 800 ka. *Quaternary Sciences* (06), 1474–1485. <https://doi.org/10.11928/j.issn.1001-7410.2020.06.09>.
- Wei, Q., 1979. Thestrigraphy and the age of the Huangshan in Harbin. *Acta Stratigraphica Sinica* 3 (3), 208–213.
- Wei, C.Y., Li, C.A., Kang, C.G., Chang, G.R., 2015. Grain-size Characteristics and Genesis of the Huangshan Loess in Songnen Plain Area. *Earth Sci.* 40 (12), 1945–1954.
- Wei, Z.Y., Xie, Y.Y., Kang, C.G., Chi, Y.P., Wu, P., Wang, J.X., Zhang, M., Zhang, Y.X., Liu, L., 2020. The Inversion of the Songhua River System in the early Pleistocene: Implications from Sr-Nd isotopic composition in the Harbin Huangshan cores. *Acta Sedimentol. Sin.* 6, 1192–1203. Doi: 10.14027 / j.i SSN. 1000-0550.2019.112.
- Wu, Z.H., 1959. Comparative study on humus properties of black soil, dark meadow soil and white pulpy soil. *Acta Pedologica Sinica* 22, 135–144.
- Wu, X.H., Pu, Q.Y., Qian, F., Sun, J.Z., Wang, Y.Z., Zhou, Y.J., Chen, S.H., Zhang, Q.Y., Zhao, G.B., He, Z.Y., Yu, H.Y., Tong, S.G., Gao, Z.C., Wang, W., 1984. Preliminary study on Quaternary magnetic stratigraphy in Songliao Plain in North-East China. *Mar. Geol. Quat. Geol.* 02, 1–13. Doi: 10.16562 / j.carol.carroll.nki.0256–1492.1984.02.001.
- Wu, B.Y., Su, J.Z., Zhang, R.H., 2011. Effects of autumn-winter Arctic Sea ice on winter Siberian High. *Chin. Sci. Bull.* 56 (30), 3220–3228. <https://doi.org/10.1007/s11434-011-4696-4>.
- Wu, Y., Qiu, S.F., Fu, S.Q., Rao, Z.G., Zhu, Z.Y., 2018. Pleistocene climate change inferred from multi-proxy analyses of a loess–paleosol sequence in China. *J. Asian Earth Sci.* 154, 428–434. <https://doi.org/10.1016/j.jseas.2017.10.007>.
- Wu, P., Xie, Y.Y., Kang, C.G., Chi, Y.P., Wei, Z.Y., Wang, J.X., Zhang, M., Zhang, Y.X., Liu, L., 2020a. The capture of the Songhua River system in the late early Pleistocene: geochemical and sedimentological records. *Geol. J.* 94 (10), 3144–3160. <https://doi.org/10.3969/j.issn.0001-5717.2020.10.024>.
- Wu, P., Xie, Y.Y., Kang, C.G., Chi, Y.P., Wei, Z.Y., Sun, L., Wang, J.X., 2020b. The Genesis of Huangshan Loess in Harbin: Integrated Evidence from Grain Size, Geochemistry, Magnetization, Sedimentation and Landform. *J. Earth Sci.* 41 (3), 420–430. <https://doi.org/10.3975/cagsb.2019.111801>.
- Wu, P., Xie, Y.Y., Chi, Y.P., Kang, C.G., Sun, L., Wei, Z.Y., Zhang, M., Zhang, Y.X., 2021. Loess accumulation in Harbin with implications for late Quaternary aridification in the Songnen Plain, Northeast China. *Palaeogeogr. Palaeoclimatol. Palaeoecol.* 570, 110365. <https://doi.org/10.1016/j.palaeo.2021.110365>.
- Wu, P., Xie, Y.Y., Li, Y., Kang, C.G., Chi, Y.P., Sun, L., Wei, Z.Y., 2022. Decoupling between circulation pattern and dust path since the last glacial in the Songnen Plain, NE China: Insights from quantitative provenance reconstruction of the Harbin dust sediments. *Aeolian Res.*, 2022, 57, 100818. doi: <https://doi.org/10.1016/j.aeolia.2022.100818>.
- Wu, P., Xie, Y.Y., Li, Y., Kang, C.G., Chi, Y.P., Sun, L., Wei, Z.Y., 2023. Provenance variations of the loess deposits in the East Asian monsoon boundary zone, Northeast China: Response to the variations of climate and wind regimes. *Catena* 222, 106804. <https://doi.org/10.1016/j.catena.2022.106804>.

- Xia, Y.M., Wang, P.F., 1987. Study on Neogene - Pleistocene palynological association, paleo-vegetation and paleoclimate in Songnen Plain. *J. Geogr.* 02, 165–178.
- Xia, Y.M., Wang, P.F., Wang, M.H., 1983. Preliminary research on spore-pollen association of the section of Huang Shan in Harbin. *Sci. Geogr. Sin.* 3 (2), 183–187.
- Xiao, L., Yao, K.H., Li, P., Liu, Y., Zhang, Y., 2020. Effects of freeze-thaw cycles and initial soil moisture content on soil aggregate stability in natural grassland and Chinese pine forest on the Loess Plateau of China. *J. Soils Sediments* 20, 1222–1230. <https://doi.org/10.1007/s11368-019-02526-w>.
- Xie, X.X., Liu, X.D., 2020. Regional differences of east Asian monsoon precipitation in response to orbital forcing and global ice-volume changes since the late middle pleistocene. *Quaternary Sciences* 06, 1486–1498. <https://doi.org/10.11928/j.issn.1001-7410.2020.06.10>.
- Xie, Y.Y., Yuan, F., Zhan, T., Kang, C.G., Chi, Y.P., Ma, Y.F., 2018. Geochemistry of loess deposits in northeastern China: constraint on provenance and implication for disappearance of the large Songliao paleolake. *J. Geol. Soc. Lond.* 175 (1), 146–162. <https://doi.org/10.1144/jgs2017-032>.
- Xie, Y.Y., Kang, C.G., Chi, Y.P., Du, H.R., Wang, J.X., Sun, L., 2019. The loess deposits in Northeast China: the linkage of loess accumulation and geomorphic-climatic features at the easternmost edge of the Eurasian loess belt. *J. Asian Earth Sci.* 181, 103914. <https://doi.org/10.1016/j.jseas.2019.103914>.
- Xie, Y.Y., Kang, C.G., Chi, Y.P., Wu, P., Wei, Z.Y., Wang, J.X., Sun, L., 2020. Reversal of the middle-upper Songhua River in the late early Pleistocene. *Northeast China. Geomorphology* 369, 107373. <https://doi.org/10.1016/j.geomorph.2020.107373>.
- Xiong, L., Liu, B., Sun, Y., 2023. Changes in global surface temperature and physical mechanisms during the last Interglacial period. *Quaternary Sciences* 43 (4), 1010–1018. <https://doi.org/10.11928/j.issn.1001-7410.2023.04.09>.
- Xu, K.K., Yang, Z.J., Ning, K., Han, Q.Q., Bi, Z.W., Zhao, N.N., 2021. Reconstruction of climatic and environmental evolution in the Yinchuan Basin from MIS6 to MIS5 based on spore-pollen evidence. *Geoscience* 35 (05), 1311–1322. <https://doi.org/10.12090/j.issn.1006-6616.2023091>.
- Xu, K.K., Yang, Z.J., Ning, K., Han, Q.Q., Bi, Z.W., Zhao, N.N., 2023. MIS6-MIS5 climate Change of Yinchuan Basin based on End-member Method. *J. Geom.* 04, 522–542. <https://doi.org/10.19657/j.geoscience.1000-8527.2021.077>.
- Yang, Y.Q., Yin, K., Wang, C.W., Zhao, L.L., Chen, S.L., Zhao, C.L., Cheng, S., Liu, Z.D., Hong, H.L., 2020. Advances of the research on quantification of hematite and goethite using diffuse reflectance spectroscopy. *Acta Mineral. Sin.* 40 (1), 92–100. <https://doi.org/10.16461/j.cnki.1000-4734.2019.39.088>.
- Yang, Y., Zhang, P.P., Song, Y., Li, Z.M., Zhou, Y.Y., Sun, H., Qiao, J.B., Wang, Y.Q., An, S.S., 2024. The structure and development of Loess critical Zone and its soil carbon cycle. *Carbon Neutrality* 3 (1), 1. <https://doi.org/10.1007/s43979-023-00076-2>.
- Ye, Q.X., 1991. Quaternary System in Harbin area. *Heilongjiang Geology* 2 (2), 17–29.
- Yi, L., Shi, Z.G., Tan, L.C., Deng, C.L., 2018. Orbital-scale nonlinear response of East Asian summer monsoon to its potential driving forces in the late Quaternary. *Clim. Dyn.* 50, 2183–2197. <https://doi.org/10.1007/s00382-017-3743-5>.
- Yu, J.Y., 1979. Soil magnetism: a new field of soil science. *Adv. Soil Sci.* 4, 1–12.
- Yu, J.Y., Zhao, W.S., Zhan, S.R., 1981. The Magnetic Susceptibility Distinction of Paddy Soils in Taihu Lake Region. In: Proceedings of Symposium on Paddy Soils. Springer, Berlin, Heidelberg, pp. 493–497. [https://doi.org/10.1007/978-3-642-68141-7\\_58](https://doi.org/10.1007/978-3-642-68141-7_58).
- Zeng, L., Lu, H.Y., Yi, S.W., Stevens, T., Xu, Z.W., Zhuo, H.X., Yu, K.F., Zhang, H.Z., 2017. Long-term Pleistocene aridification and possible linkage to high-latitude forcing: New evidence from grain size and magnetic susceptibility proxies from loess-paleosol record in northeastern China. *Catena* 154, 21–32. <https://doi.org/10.1016/j.catena.2017.02.020>.
- Zhan, T., Zeng, F.M., Xie, Y.Y., Yang, Y., Ma, Y.F., Ge, J.Y., Yi, L., Chi, Y.P., Kang, C.G., Jiang, X., Zhang, J., Lou, B.J., Zhou, X., Deng, C.L., 2018. Grain size characteristics of tianhengshan core and their indications for stratigraphic division in the eastern part of the northeast plain of China. *J. Geom.* 24 (4), 515–521. <https://doi.org/10.12090/j.issn.1006-6616.2018.24.04.054>.
- Zhan, T., Zeng, F.M., Xie, Y.Y., Yang, Y., Ge, J.Y., Ma, Y.F., Chi, Y.P., Kang, C.G., Jiang, X., Yu, Z.Y., Zhang, J., Li, E., Zhou, X., 2019. Magnetostratigraphic dating of a drill core from the Northeast Plain of China: Implications for the evolution of Songnen paleo-lake. *Chin. Sci. Bull.* 11, 1179–1190. <https://doi.org/10.1360/N972018-01212>.
- Zhang, Y.G., Ji, J.F., Balsam, W.L., Liu, L.W., Chen, J., 2007. High resolution hematite and goethite records from ODP 1143, South China Sea: co-evolution of monsoonal precipitation and El Niño over the past 600,000 years. *Earth Planet. Sci. Lett.* 264 (1–2), 136–150. <https://doi.org/10.1016/j.epsl.2007.09.022>.
- Zhang, Y.X., Chi, Y.P., Xie, Y.Y., Kang, C.G., Wu, P., Wei, Z.Y., Zhang, M., Liu, L., 2020. Organic Carbon Isotope Composition of Harbin Loess since the Mid-Pleistocene and its Paleoclimatic significance. *J. Earth Sci.* 04, 525–534. <https://doi.org/10.3975/cagsb.2020.040602>.
- Zhang, M., Xie, Y.Y., Kang, C.G., Chi, Y.P., Wu, P., Wei, Z.Y., Zhang, Y.X., Liu, L., 2021. Chemical Weathering Characteristics of the Loess-Paleosol Sequences in Harbin Huangshan Rock Core—Implication for Formation Environment of the Paleosol. *Acta Pedol. Sin.* 58 (3), 673–684. <https://doi.org/10.11766/trxb201910080472>.
- Zhang, X.R., Xie, Y.Y., Chi, Y.P., Kang, C.G., Sun, L., Wu, P., Wei, Z.Y., 2023a. Heavy mineral compositions in the northeast sandy lands and the provenance analysis. *Mar. Geol. Quat. Geol.* 43 (6), 181–190. <https://doi.org/10.16562/j.cnki.0256-1492.2022110501>.
- Zhang, Y., Xu, J.S., Li, G.X., Lu, Z.Y., Jiang, Z.X., Zhang, W.C., Liu, Y., 2023b. ENSO-like evolution of the tropical Pacific climate mean state and its potential causes since 300ka. *Quat. Sci. Rev.* 315, 108241. <https://doi.org/10.1016/j.quascirev.2023.108241>.
- Zhang, Y.Y., Chi, Y.P., Xie, Y.Y., Kang, C.G., Liu, R.N., Sun, L., Wu, P., Wei, Z.Y., 2024. Characteristics and climate significance of surface sediments in the Horqin Sandy Land. *J. Desert Res.* 44 (4), 223–235. <https://doi.org/10.7522/j.issn.1000-694X.2024.00043>.
- Zhao, J., Lu, H.Y., Wang, X.Y., Zhang, H.Y., Wang, S.J., 2008. Magnetic Properties of Loess Deposit in Eastern Qinling Mountains and An Investigation on the Magnetic Susceptibility Enhancement. *26 (6)*, 1052–1062.
- Zhao, Q., Xie, Y.Y., Hao, D.M., Chi, Y.P., Kang, C.G., Wu, P., Liu, S., 2022. Climatic Aridification in Songnen Plain since the Middle Pleistocene from Harbin Loess Records Journal of deposition (6), 1702–1717. Doi: 10.14027 / j.i SSN. 1000-0550.2021.054.
- Zhao, D.B., Lu, Z.Y., Wan, S.M., Cheng, H., Shi, X.F., Li, A., 2023. Quaternary rainfall variability is governed by insolation in northern China and ice-sheet forcing in the south. *Communications Earth Environment*, 4(1), 7. doi: <https://doi.org/10.1038/s43247-022-00670-9>.
- Zhao, H., Qiang, X.K., Xu, X.W., Zhang, P., Quan, C.Y., Chang, D., Zhao, C., Ao, H., Xu, X. L., 2024. Goethite in the Red Clay sequences on the western Chinese Loess Plateau and its responses to the middle Miocene climate transition. *Catena* 237, 107798. <https://doi.org/10.1016/j.catena.2023.107798>.
- Zhou, L.P., Oldfield, F., Wintle, A.G., Robinson, S.G., Wang, J.T., 1990. Partly pedogenic origin of magnetic variations in Chinese loess. *nature* 346 (6286), 737–739. <https://doi.org/10.1038/3467370>.
- Zhou, Y., Sun, L., Xie, Y.Y., Kang, C.G., Wei, C.Y., Wang, Y.H., Wei, Z.Y., Wu, P., Liu, H.J., 2025. Evolution of the East Asian Summer Monsoon in the Songnen Plain, NE China since 195 ka recorded by the Harbin loess succession. *Catena* 259, 109343. <https://doi.org/10.1016/j.catena.2025.109343>.
- Zhu, M.Y., Lü, B., Guo, Y., 2022. Comparison of Haematite and Goethite Contents in Aeolian Deposits in different climate zones based on Diffuse Reflectance Spectroscopy and Chromaticity Methods. *Spectrosc. Spectr. Anal.* 42 (06), 1684–1690. [https://doi.org/10.3964/j.issn.1000-0593\(2022\)06-1684-07](https://doi.org/10.3964/j.issn.1000-0593(2022)06-1684-07).
- Zhu, X.R., Xu, X.Y., Jia, G.S., 2024. Contribution of Northern Hemisphere high latitude permafrost region to global wildfire emissions. *Sci. China Earth Sci.* 10, 3292–3304. <https://doi.org/10.1007/s11430-024-1397-2>.